Environmental Research Center Papers

Number 7

1985

Environmental Research Center
The University of Tsukuba

MODELLING AND CLIMATOLOGICAL ASPECTS OF CONVECTIVE BOUNDARY LAYER*

By Chong Bum LEE**

(received February 27, 1985)

ABSTRACT

A model which estimates the parameters in the convective boundary layer using routine meteorological observation data is developed. The data required are net radiation, air temperature, wind speed, and radiosonde sounding. The model includes the estimation schemes of surface heat flux and friction velocity, and a mixed layer height model modified from the jump model.

The jump model is modified for mechanical convection and large scale vertical motion. A sensitivity test shows the importance of mechanical convection and large scale vertical motion.

The field observation of the boundary layer was carried out at Tsukuba. The field observation data are used to determine empirical equation of the surface heat flux and to evaluate the model. Estimated values of the surface heat flux using the empirical equation fit well with observed values. Evaluation of the scheme, which estimates the friction velocity and the Monin-Obukhov length, shows that the scheme can be adopted for the purpose of the present study. From the results of evaluation using the data set of the Wangara experiment and the field observation at Tsukuba, it has been shown that the modification of the jump model improves results.

Seasonal and diural variations of the convective boundary layer are obtained using the model for data over a period of three years at Tsukuba.

Stability of the surface layer is most unstable in autumn. However, in the boundary layer, the stability is most unstable in spring. Convection is most intensive in spring. There are two peaks in the seasonal variation pattern of the mixed layer height occurring in spring and autumn. Notably, it is not so high in summer in spite of strong solar radiation.

It is known that the potential temperature gradient is large in summer and small in winter, with this feature being related to air mass types. The potential temperature gradient of continental air mass is small and that of maritime air mass is large. The development of the mixed layer is closely related to the potential temperature gradient, and is surpressed by a strong inversion layer, especially in summer. Thus together with the surface heat flux, the occurence frequency of types of air mass is one of the important factors in explaining seasonal variation of the structure of the convective boundary layer.

---

* A dissertation submitted for the degree of Doctor of Science in the University of Tsukuba.

** Address: Department of Environmental Science, Kangwon National University, Chuncheon 200, Korea.

CONTENTS

ABSTRACT 1

LIST OF FIGURES 4

LIST OF TABLES 6

LIST OF SYMBOLS 7

CHAPTER I INTRODUCTION 9
1.1 Review of previous studies 9
1.2 Purposes of the present study 11

CHAPTER II MODELLING THE STRUCTURE OF CONVECTIVE BOUNDARY LAYER 12
2.1 Modelling of mixed layer height 12
2.1.1 Modifications of mixed layer height model 12
2.1.2 Sensitivity of mixed layer height model 15
2.1.3 Evaluation of mixed layer height model with Wangara experiment data. 17
2.2 Estimation of surface flux 19
2.2.1 Surface heat flux 19
2.2.2 Friction velocity and Monin-Obukhov length 22
2.3 Turbulence terms 24

CHAPTER III EVALUATION OF CONVECTIVE BOUNDARY LAYER MODEL WITH FIELD OBSERVATION AT TSUKUBA 27
3.1 Details of field observation 27
3.2 Empirical equation of surface heat flux 29
3.3 Evaluation of the estimation scheme of friction velocity and Monin-Obukhov length 30
3.4 Evaluation of mixed layer height model 31
3.5 Standard deviations of vertical velocity and temperature 33
3.6 Discussions on accuracy of the model applied to climatological study of convective boundary layer 35

CHAPTER IV CLIMATOLOGICAL ASPECTS OF CONVECTIVE BOUNDARY LAYER 36
4.1 Methods 36
4.2 Data and limitations imposed by weather conditions 39
4.3 Seasonal variation of structure of convective boundary layer 40
4.4 Evolution of convective boundary layer in daytime 44
4.5 Relationships between structure of convective boundary layer and synoptic conditions 48

CHAPTER V CONCLUSIONS 53

ACKNOWLEDGEMENTS 55

REFERENCES 56

APPENDIX 58

LIST OF FIGURES

Fig. 1 Schematic diagram of the profiles of potential temperature and heat flux distribution of the jump model 13
Fig. 2 Variation of γ due to large scale subsidence 14
Fig. 3 The effects of h_0, a, u_*, and w_h on the variation of h in time 16
Fig. 4 Comparison between h_{obs} and h_{MJM} using the Wangara experiment data 17
Fig. 5 Relationship between λ/s and α'' 21
Fig. 6 Flow chart of the estimation scheme for u_* and L 23
Fig. 7 Map of the observation site and surroundings 27
Fig. 8 Comparison of H_{obs} with H_{est} according to Eq. (40) 30
Fig. 9 Comparison of daytime mean value of H_{obs} with that of H_{est} 30
Fig. 10 Comparison of u_{*obs} with u_{*est} according to the scheme described in 2.2.2 31
Fig. 11 Same as Fig. 10, but for L 31
Fig. 12 Development of the mixed layer under convective condition 32
Fig. 13 Same as Fig. 12, but for the case of mechanical convection 32
Fig. 14 Comparison between h_{obs} and h_{MJM} using the data observed at Tsukuba 33
Fig. 15 Comparison of observed σ_{ws} (σ_{wsobs}) with the estimated values (σ_{wsest}) by Eq. (26) 34
Fig. 16 Comparison of observed σ_{Ts} (σ_{Tsobs}) with the estimated values (σ_{Tsest}) by Eq. (27) 34
Fig. 17 The scheme of determination of $\gamma_{500\text{-}1500}$ 37
Fig. 18 Typical examples of pressure patterns and potential temperature profiles for the six air mass types 38
Fig. 19 Seasonal variations of surface heat balance components in daytime 41
Fig. 20 Seasonal variations of u_* and w_* 41
Fig. 21 Seasonal variation of z/L expressed by 25 and 75 percentiles, and the median 42
Fig. 22 Same as Fig. 21, but for h/L 42
Fig. 23 Seasonal variation of h expressed by 10 and 90 percentiles, and the median 42
Fig. 24 Same as Fig. 23, but for σ_{ws} 42
Fig. 25 Same as Fig. 23, but for σ_{Ts} 43
Fig. 26 Same as Fig. 23, but for σ_{wb} 43
Fig. 27 Same as Fig. 23, but for σ_{Tb} 43
Fig. 28 Same as Fig. 23, but for K_m 43
Fig. 29 Same as Fig. 23, but for K_h 45
Fig. 30 Diurnal variation of u_* for selected months; Feb., May, Aug., and Nov. 45
Fig. 31 Same as Fig. 30, but for w_* 45

Fig. 32 Same as Fig. 30, but for z/L 45
Fig. 33 Same as Fig. 30, but for h/L 46
Fig. 34 Same as Fig. 30, but for h 46
Fig. 35 Same as Fig. 30, but for σ_{ws} 46
Fig. 36 Same as Fig. 30, but for σ_{Ts} 46
Fig. 37 Same as Fig. 30, but for σ_{wb} 47
Fig. 38 Same as Fig. 30, but for σ_{Tb} 47
Fig. 39 Same as Fig. 30, but for K_m 47
Fig. 40 Same as Fig. 30, but for K_h 47
Fig. 41 Seasonal variation of $\gamma_{500\text{-}1500}$ 49
Fig. 42 Relative frequencies of the six air mass types 49
Fig. 43 Mean values of $\gamma_{500\text{-}1500}$ for the six air mass types 50
Fig. 44 Mean profile of the potential temperature gradient for the air mass type which has the highest frequency in a month 51
Fig. 45 Comparison of parameters in the convective boundary layer between fair weather conditions and cloudy conditions 52

LIST OF TABLES

Table 1 Reference conditions for the sensitivity test of the mixed layer height model 15

Table 2 Comparisons of the mixed layer height between calculated values with reference conditions and with changing conditions 16

Table 3 Sky conditions and w_h in the Wangara experiment data selected for analysis 18

Table 4 Comparison of h_{obs} with h_{MJM}, h_{JM}, and h_{HOL} using the Wangara experiment data 19

Table 5 Comparison between monthly mean α'' and λ/s 20

Table 6 Brief description of meteorological elements and instruments of the observation performed using the 213 m meteorological tower at the Meteorological Research Institute 28

Table 7 Period of the tower observation 28

Table 8 Summary of low level sonde observation 29

Table 9 Comparison of estimated values with observed values for u_* and L 31

Table 10 Comparison of h_{obs} with h_{MJM}, h_{JM} and h_{HOL} using the field observation data at Tsukuba 33

Table 11 Comparison between observed values and estimated values for σ_{ws} and σ_{Ts} 34

Table 12 Number of days for climatological analysis of the convective boundary layer over 3 years; 1980 – 1982 40

Table 13 Maximum and minimum values among medians for 12 months 44

Table 14 Mean developing rate of the mixed layer from 09:30 LST to 14:30 LST 48

LIST OF SYMBOLS

Roman alphabet

A	amplitude of B
a	amplitude of diurnal variation of heat flux
B	diurnal variation term of α''
b	empirical constant
C_e	entrainment ratio
c_1, c_2, c_3	empirical constant
c_p	specific heat of air at constant pressure
D	nondimensional constant
d	number of days counted from the winter solstice
G	soil heat flux
g	acceleration of gravity
H	surface heat flux
h	mixed layer height
h_{HOL}	mixed layer height estimated by Holzworth's scheme
h_{JM}	mixed layer height calculated by jump model
h_{MJM}	mixed layer height calculated by modified jump model
h_r	mixed layer height calculated with reference conditions in the sensitivity test
h_0	initial value of the mixed layer height
K_h	exchange coefficient for heat
K_m	exchange coefficient for momentum
k	Von Karman constant
L	Monin-Obukhov length
LE	latent heat flux
p	amplitude of variation of time of sunrise
q	time of sunrise at the vernal equinox
q_s	saturation specific humidity
Rn	net radiation
s	slope of the saturation specific humidity temperature curve
T	air temperature
T_*	scaling temperature in the surface layer
t	time
t_d	length of daytime
t_r	time of sunrise
t_t	transit time of sun
u	wind speed
u'	fluctuating component from mean wind speed
u_z	wind speed at height z
u_*	friction velocity
w'	fluctuating component from mean vertical wind speed

w_h	large scale vertical velocity at the top of the mixed layer
w_*	scaling velocity in the planetary boundary layer
x	defined as $x = [1 - 16(z/L)]$
z	height
z_i	height of inversion base
z_0	roughness length

Greek alphabet

$\alpha, \alpha', \alpha''$	parameters depend on the soil moisture condition
γ	potential temperature gradient above the mixed layer
γ_0	initial value of potential temperature gradient
$\gamma_{500\text{-}1500}$	mean potential temperature gradient between 500 m and 1,500 m
$\Delta\theta$	potential temperature jump at the top of the mixed layer
$\Delta\theta_0$	initial value of potential temperature jump
θ	potential temperature
θ'	fluctuating component from mean potential temperature
θ_*	scaling temperature in the boundary layer
ψ_m	stability function
λ	psychrometric constant
ρ	density of air
ϕ_h	nondimensional temperature gradient function
ϕ_m	nondimensional wind gradient function
σ_{Tb}	standard deviation of temperature in the convective boundary layer
σ_{Ts}	standard deviation of temperature in the unstable surface layer
σ_{wb}	standard deviation of vertical velocity in the convective boundary layer
σ_{ws}	standard deviation of vertical velocity in the unstable surface layer

Subscript

est	indicating estimated value
obs	indicating observed value

CHAPTER I

INTRODUCTION

1.1 Review of previous studies

The planetary boundary layer is located in the lower part of the tropopause ranging up to a height of 1 – 2 km. Its structure varies widely over the course of a diurnal cycle. In the lower part of the planetary boundary layer, from the surface to a few ten m, there is the surface layer. Diurnal variation of meteorological variables in the surface layer are remarkably larger than above. This layer is often called the constant flux layer because the flux is regarded as almost constant with height.

Knowledge of the boundary layer structure is required for many purposes; for example, to estimate the dispersion of atmospheric pollutants and also for incorporation into numerical forecasting and general circulation models. In order to describe the causes of climatological characteristics near the ground surface, information about the planetary boundary layer structure may also be required.

The planetary boundary layer is divided into 3 types according to stability; convective boundary layer in the daytime, stable boundary layer at night, and neutral boundary layer which occurs transiently.

During the night, when the air in contact with the ground is cooled, a nocturnal inversion is formed. As the sun rises in the morning, convection develops which tends to mix the air close to the ground surface. A convective boundary layer with an upward heat flux from the surface is generally capped by an inversion layer. As the boundary layer heats up during the course of a sunny day, the inversion layer base rises gradually due to action of turbulence in the boundary layer, which entrains warm air from above the inversion layer base.

The potential temperature of a well developed convective boundary layer is kept constant with height by vertical mixing. In general, this layer is called the mixed layer.

There are several parameters used to describe the structure of the convective boundary layer and among these, mixed layer height is one of the most fundamental parameters.

Holzworth (1964) proposed a scheme which can estimate the maximum mixed layer height in the daytime utilizing morning radiosonde sounding and daily maximum temperature. The maximum mixed layer height is often called the MMD; maximum mixing depth. Holzworth (1964) analysed the MMD for 45 stations in the contiguous U.S.A. for 10 years using this scheme, and showed spacial distributions and annual variation patterns of the MMD.

In order to investigate the relationship between the MMD and the concentration of SO_2, Sugiura (1972) analized the MMD determined by Holzworth's scheme for Tokyo and its surroundings.

Gamo (1981, 1983) studied the seasonal variation of the MMD at Tsukuba, Japan with Holzworth's scheme, and showed that the MMD varies significantly throughout the year: highest in February, lowest in December and relatively low in summer. Gamo (1983) explained that this seasonal variation is related to frequency of air mass types and seasonal variation of the surface heat flux.

Benkley and Schulman (1979) modified Holzworth's scheme by considering the temperature advection term, and showed results improved by modification.

Norton and Hoidale (1976) studied diurnal variation of the mixed layer height at while Sands Missile Range. Since radiosondes were released at various times during the day, details of the diurnal variation of the mixed layer height could be obtained from radiosonde data alone.

Ways of predicting the rate of the mixed layer development have been formulated by many investigators. Ball (1960) first described the development of the mixed layer using the concept of a temperature jump at the top of the mixed layer. The "0-order jump model" has been improved upon by many authors (Lilly, 1968; Carson, 1973; Tennekes, 1973). Generally, the 0-order jump model is simply called the jump model.

The jump model can estimate the mixed layer height in the daytime by considering the entrainment and temperature jump at the top of the mixed layer. Entrainment is caused by penetrative convection into the stable layer above and the temperature jump is controlled by the potential temperature gradient in the stable layer.

The ratio of downward heat flux at the inversion base to the surface heat flux, entrainment ratio, varies widely from 0 to 1 (Ball, 1960; Deardorff, 1972, 1973; Lilly, 1968; Lenschow and Johnson, 1968; Carson, 1973; Cattle and Weston, 1974). Parameterizations of the entrainment ratio have been suggested by many authors (Stull, 1973, 1976; Driedonks, 1982).

The jump model requires the surface heat flux as input data. This can be obtained by the heat balance method using the Bowen ratio, or by the flux-profile method (Paulson, 1970; Panofsky, 1971) using the temperature and the wind speed profiles. These methods require data which can not be obtained from routine meteorological observations.

Another approach, which can estimate the latent heat flux and thus can estimate the surface heat flux, was given by Monteith (1981). Following Monteith, the surface latent heat flux can be obtained from net radiation, soil heat flux, aerodynamic resistance, surface resistance, and specific humidity. This approach is complicated, and several input parameters which are not available from routine meteorological observations are needed.

Priestley and Taylor (1972) propose a simple equation which can estimate the surface heat flux by using net radiation and temperature. De Bruin and Holtslag (1982) modified this equation and obtained good agreement with observed values in the Netherlands.

Turbulent characteristics in the convective boundary layer can be expressed by the surface heat flux, the friction velocity, and the mixed layer height.

Panofsky *et al.* (1977) recommended a formula which can well express the variance of vertical velocity in the surface layer for unstable conditions using the Monin-Obukhov length and the friction velocity.

Variance of temperature in the surface layer under unstable conditions can be expressed as a function of the Monin-Obukhov length and the heat flux. Wyngaard *et al.* (1971) determined an empirical constant in this formula using the Kansas data.

Variances of vertical velocity and temperature in the convective boundary layer are functions of the mixed layer height. Caughey and Palmer (1979) have summarized these relationships.

Gamo (1983) obtained seasonal variations of velocity scale and variance of vertical velocity in the boundary layer at Tsukuba. In the calculation, Gamo used the MMD determined by Holzworth's scheme, and also used the surface heat flux estimated from the morning potential temperature profile and the MMD.

Fujitani (1983) analysed a seasonal variation of thermal diffusivity. Since Fujitani used daily temperature range as input data, results show only aproximated values during a day.

1.2 Purposes of the present study

There is only limited literature concerning climatological study of the convective boundary layer, because schemes, which can estimate boundry layer parameters with routine meteorological observation data, are not readily available.

The purposes of the present study are to develop a model which can estimate the structure of the convective boundary layer, consisting of elements such as the mixed layer height, stability, variances, and exchange coefficients using routine meteorological observation data, and also to investigate climatological aspects of the convective boundary layer using the developed model.

The daily maximum mixed layer height can be estimated with Holzworth's scheme. This scheme is simple to apply, but results contain a large margin of error.

On the other hand, the jump model is able to estimate not only daily maximum mixed layer height, but also developing features throughout the daytime. It has been shown that the mixed layer height estimated by the jump model, using a constant value of the entrainment ratio, may be fit well with observed value in convective case. However, when the mechanical convection increases, the entrainment ratio becomes large and this factor can not be ignored. On the other hand, large scale vertical motion affects the development of the mixed layer. In the present study, we modify the jump model to incroporate mechanical convection and large scale vertical motion.

Knowledge of the surface heat flux is required for many purposes. For example, it may be used to describe the convective boundary layer, to estimate the stability of the air near the ground, to determine the input of heat from the ground into the atmosphere for weather forcast purposes, and to estimate evaporation from the ground surface.

In the present study, the surface heat flux and the friction velocity are required not only as input data of the mixed layer height model, but also as the basic parameters used to describe the structure of the convective boundary layer. The friction velocity can be estimated by the flux-profile relationship (Businger *et al.*, 1971; Paulson, 1970). However, this method requires temperature and wind speed data for at least two levels in the lower part of the surface layer. For the purpose of the present study, this method can not be applied directly, because input data are not observed routinely. We consider schemes that can estimate the surface heat flux and the friction velocity using routine meteorological observation data only.

Turbulence statistics can be obtained with empirical relationships derived earlier by many investigators. These empirical formulas are discussed by comparison with the observed data.

We perform field observation of the boundary layer at Tsukuba, Japan. Using these observation data, the model is evaluated.

In order to investigate the climatological aspects of the convective boundary layer, the model is applied for a period covering three years at Tsukuba. Seasonal and diurnal variation of the convective boundary layer will be shown together with discussions of relationships between structure of the convective boundary layer and the synoptic conditions.

CHAPTER II

MODELLING THE STRUCTURE OF CONVECTIVE BOUNDARY LAYER

2.1 Modelling of mixed layer height

2.1.1 Modifications of mixed layer height model

In the jump model, the vertical profiles of potential temperature, specific humidity and momentum are taken independent of height in the mixed layer. The jump model ignores horizontal advection and both radiational cooling and heating, and assumes that the potential temperature gradient above the mixed layer, remains constant in the daytime. These assumptions in the model lead to simplified budgets for heat, momentum, and moisture, in the mixed layer, supplemented by jump conditions at the top of the mixed layer.

Because of its simplicity, this model is widely used to estimate the mixed layer height in the daytime. Basic equations of the model are as follows,

$$\frac{d\theta}{dt} = \frac{(\overline{w'\theta'})_s - (\overline{w'\theta'})_h}{h} \tag{1}$$

$$\frac{d\Delta\theta}{dt} = \gamma \frac{dh}{dt} - \frac{d\theta}{dt} \tag{2}$$

$$\frac{dh}{dt} = \frac{(\overline{w'\theta'})_h}{\Delta\theta} \tag{3}$$

$$(\overline{w'\theta'})_h = -C_e(\overline{w'\theta'})_s , \tag{4}$$

where θ and θ' are the mean and the fluctuating component from the mean value of potential temperature respectively, w' the fluctuating component from the mean value of vertical wind speed, t the time, h the mixed layer height, $\Delta\theta$ the potential temperature jump assumed to occur at the top of the mixed layer, γ the potential temperature gradient above the mixed layer, and Ce the entrainment ratio. The overbar indicates an ensemble average and the subscripts s and h refer to the values at the surface and top of the mixed layer, respectively. In order to take into consideration the water vapor effect, the virtual potential temperature is frequently used rather than the potential temperature. However for simplicity, the potential temperature is used in the present study. Fig. 1 shows a schematic diagram of vertical profiles of potential temperature and heat flux in the jump model.

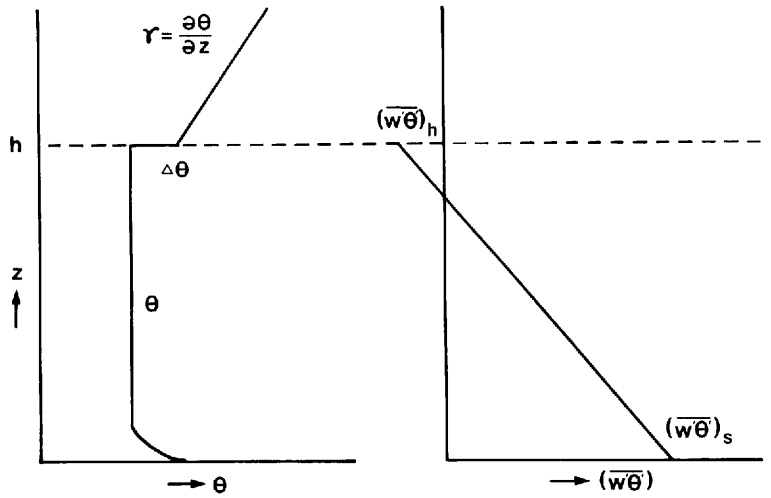

Fig. 1 Schematic diagram of the profiles of potential temperature and heat flux distribution of the jump model.

The surface heat flux H is expressed as

$$H = \rho c_p (\overline{w'\theta'})_s \,, \tag{5}$$

where ρ is the density of air and c_p the specific heat of air at constant pressure.

In general, at $C_e = 0.2$ this model agrees well with observations for convective cases with clear and light wind conditions (Yamada and Berman, 1979; Driedonks, 1982). However, under windy conditions, mechanical convection generated by wind shear increases and C_e can not remain constant. Since the downward heat flux at the top of the mixed layer can not be easily determined, it must be parameterlized with data which is readily available.

Large scale vertical motion, such as subsidence in a high pressure system or upward motion in a low pressure system, affects growth of the mixed layer. For simplicity, in most case these effects have been ignored (Driedonks, 1982). However large scale vertical motion, in the range of a few cm/sec, may have an effect on h with an order of several hundred meters as will be shown in 2.1.2.

In order to generalize the jump model so that it can be applied to varying weather conditions, it is necessary to parameterize C_e, and to modify the effect of large scale vertical motion.

In most cases, C_e lies between 0.1 and 0.2 (Stull, 1976). In the last few years, several attemps have been made to parameterize downward heat flux at the top of the mixed layer (Stull, 1976). However, since input parameters are difficult to obtain, these parameterizations can not be applied to the present study.

Simple entrainment formulation, with which growth of the mixed layer can be described well even when mechanical turbulence prevails, was presented by Driedonks (1982);

$$C_e = -(0.2 + \frac{5u_*^3 T}{gh(\overline{w'\theta'})_s}) \,, \tag{6}$$

where u_* is the friction velocity, T the air temperature, and g the gravitational acceleration. In the present study this entrainment formula is adopted and evaluated by using observational data.

Considering the effects of large scale vertical motion on development velocity of the mixed layer, Eq. (3) is written as

$$\frac{dh}{dt} = -\frac{(\overline{w'\theta'})_h}{\Delta\theta} + w_h \ , \tag{7}$$

where w_h is large scale vertical velocity at the top of the mixed layer.

The other effect of large scale vertical motion on growth of the mixed layer is modification of the initial profile of potential temperature (Mahrt and Lenschow, 1976). Potential temperature of an air parcel remains constant despite downward or upward motion. Therefore, if it is assumed that vertical velocity is different at two levels, γ is changed by large scale vertical motion (Fig. 2). Thus γ is a function of w_h and time. When w_h is large, this effect can not be ignored.

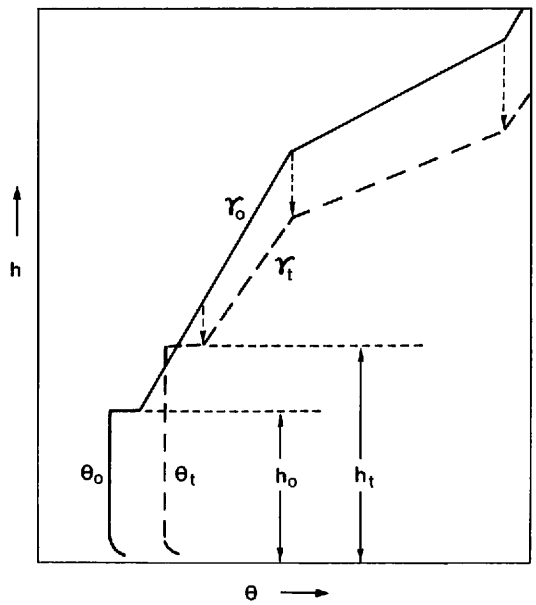

Fig. 2 Variation of γ due to large scale subsidence. Subscript 0 represents the initial value and t indicates the subsequent time value.

In the present study, mechanical turbulence and large scale vertical motion are considered in the modification of the jump model. For simplicity, it is assumed that w_h is zero at the surface, and increases linearly with height.

Limitations of the model are as follows:

(1) Diabatic heating by condensation can not be incorporated, since this model assumes that the temperature lapse rate follows the dry adiabatic lapse rate in the mixed layer, *i.e.*, potential temperature is constant with height.

(2) Effects of the horizontal advection are ignored.

(3) Cooling and heating by radiation in the mixed layer are not considered, because it is difficult to determine radiational effects, and because it is thought that cooling due to long wave radiation is somewhat compensated in the daytime by heating of short wave radiation.

(4) Since C_e is proportional to u_*^3 in Eq. (6), when u_* is large, the entrainment rate becomes very large. This may introduce a large error in h, thus the case of a strong wind is not handled in calculation.

2.1.2 Sensitivity of the mixed layer height model

In the preceeding section, to adjust for the effects of mechanical convection and large scale vertical motion, the jump model is modified. Solutions of this modified jump model (hereafter referred to as MJM) are influenced by initial conditions such as the initial mixed layer height h_0, initial potential temperature jump $\Delta\theta_0$, initial potential temperature gradient γ_0, and boundary conditions such as H, u_*, and w_h.

We have analyzed the sensitivities of the MJM for these conditions. Calculation error due to the inaccuracy of input data that inevitably arises from the atmospheric observations is discussed together with the results of the sensitivity test.

Reference conditions, used to calculate reference mixed layer height h_r are listed in Table 1.

Table 1 Reference conditions for the sensitivity test of the mixed layer height model.

h_0	=	100 m
$\Delta\theta_0$	=	0.5°K
γ_0	=	0.005°K/m
T	=	280°K
w_h	=	0 m/s
u_*	=	0 m/s
$(\overline{w'\theta'})_S$	=	$a \sin \pi t/12$
a	=	0.15°K m/s

The heat flux from the surface is assumed to be a sine function.

Calculation is performed for reference conditions, and then for changing conditions, in the order shown in Table 2. We calculate h for 7 hours starting at 08:30 LST.

Fig. 3 is a comparison between h_r and h calculated with changing conditions. Initial conditions, h_0 and $\Delta\theta_0$, are difficult to determine with initial potential temperature profile. However, the model is insensitive to these values and effects due to inaccuraces of h_0 and $\Delta\theta_0$ become negligible after the first hour.

Since mechanical effects caused by wind shear are large when h is low (Driedonks, 1982), this effect varies with time. In the morning hours, the developing rate of h under the condition of $u_* = 0.5$ m/s is much greater in comparison to reference conditions. However the difference decreases gradually.

Table 2 Comparisons of the mixed layer height between calculated values with reference conditions and with changing conditions. The mixed layer heights are expressed with values after 7 hours run.

Condition	h (m)	$h - h_r$ (m)	$\frac{(h - h_r)}{h_r} 100$ (%)
A	1,094	7	0.6
B	1,074	−13	−1.2
C	986	−101	−9.3
D	971	−116	−10.7
E	1,264	177	16.3
F	1,233	146	13.4
G	1,416	329	30.4

Notes;

h_r mixed layer height calculated with reference conditions; 1,087 m

h mixed layer height calculated with changing conditions as A–G

A Same as reference conditions but, for h_0=200 m

B Same as reference conditions but, for $\Delta\theta_0$=1.0°K

C Same as reference conditions but, for γ_0=0.006°K/m

D Same as reference conditions but, for a=0.12°K m/s

E Same as reference conditions but, for u_*=0.5 m/s

F Same as reference conditions but, for w_h=0.01 m/s at 1,000 m

G Same as reference conditions but, for u_*=0.5 m/s and w_h=0.01 m/s at 1,000 m

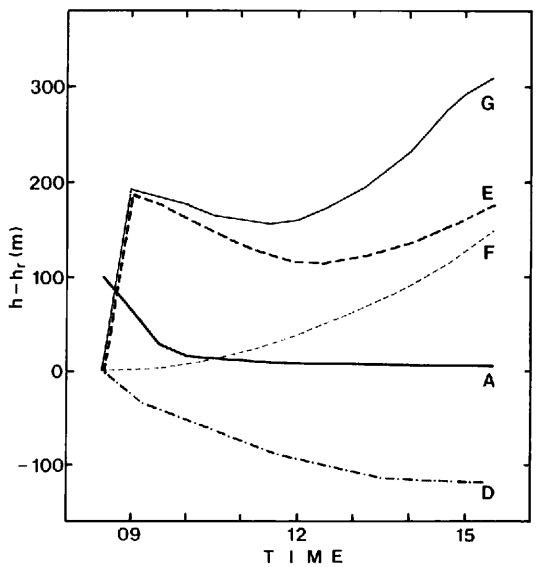

Fig. 3 The effects of h_0, a, u_*, and w_h on the variation of h in time. The ordinate expresses $h-h_r$. Values of h are calculated according to the conditions of A, D, E, F, and G given in Table 2.

A change of 20% in H causes a difference of about 10% in h (Table 2). Gamo and Yokoyama (1979) showed that mixed layer height is roughly propotional to the square root of heat flux, similar to the result obtained here. In order to estimate h within 10% error, it is necessary to estimate h within an error of less than 20%.

When large scale upward motion occurs at 1,000 m at a rate of 1 cm/s, h becomes 146 m higher than h_r after 7 hours run. Assuming that two conditions, $u_* = 0.5$ m/s and $w_h = 1$ cm/s, occur simultaneously, h becomes 329 m higher than h_r. Thus, it is important to consider large scale vertical motion and mechanical convection terms in the jump model.

2.1.3 Evaluation of mixed layer height model with Wangara experiment data

Evaluation of the MJM is carried out, using the Wangara experiment data (Clark *et al.*, 1971).

The Wangara experiment was conducted in a large area of sparsely vegetated, flat terrain located near Hay, Australia, during July and August 1967. Temperature, pressure and humidity profiles were obtained from radiosondes released every 3 hours to a height of 2,000 meters.

From the 41 days of published data, 20 days are selected for analysis here. Days with significant precipitation, low level cloud amount over 50%, and synoptic scale disturbances were excluded. A list of the selected 20 days is given in Table 3.

The observed mixed layer height h_{obs} is determined twice a day from potential temperature profiles at 12:00 and 15:00 LST.

In order to provide initial conditions, radiosonde soundings at 09:00 LST are used. The data of w_h determined from pilot baloon observations are also used.

Since H determined by the eddy correlation method are relatively scarce in the data book, H and u_* are estimated by the flux-profile method (Paulson, 1970). In practical calculation, temperatures and wind speeds at two levels, 1 m and 4 m are used. Values of intermediate times are obtained by linear interpolation of successive hourly values.

Model calculation is started at 09:00 LST. We compare h calculated by the MJM, h_{MJM}, and h calculated by the jump model, h_{JM}, with h_{obs} (Fig. 4). It has been demonstrated that modifica-

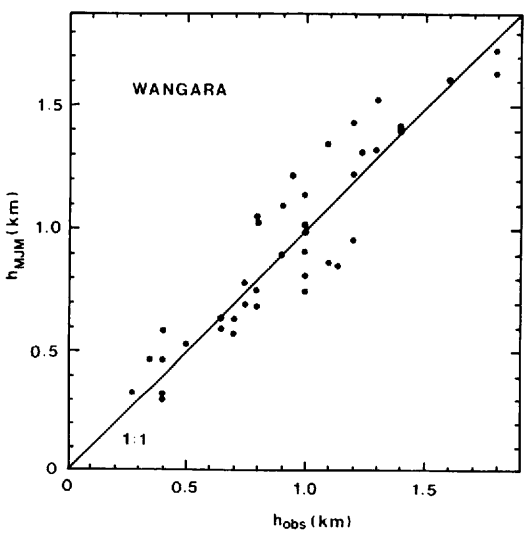

Fig. 4 Comparison between h_{obs} and h_{MJM} using the Wangara experiment data.

tions for mechanical turbulence and large scale vertical motion improve results (Table 4). We show h determined by Holzworth's scheme, h_{HOL}, using the air temperature at 12:00 and 15:00 LST together in Table 4.

Table 3 Sky conditions and w_h in the Wangara experiment data selected for analysis. Sky conditions listed are for data at 12:00 LST, and values of w_h are averaged with hourly data between 09:00 and 15:00 LST at 2,000 m.

No.	Day No.*	w_h (cm/s)	Sky condition		
			Cloud amount (Okt.)		Type
			Low cloud	Total	
1	3	1.27	0.3	2.0	*Cs*
2	4	−0.96	3.0	4.2	*Cu, Ci*
3	6	0.05	1.8	2.5	*Cu, Ac*
4	7	−1.33	0.0	5.8	*Ci*
5	8	1.61	2.3	2.3	*Cu*
6	9	0.28	3.2	3.6	*Cu*
7	11	−0.03	3.8	3.8	*Cu*
8	12	−0.83	0.0	0.7	*Ac*
9	13	−1.19	0.0	0.0	–
10	14	−1.14	1.0	5.4	*Ac, Ci*
11	18	−1.82	4.8	4.8	*Cu*
12	31	0.10	1.8	1.8	*Cu*
13	32	−0.67	3.8	3.8	*Cu*
14	33	−0.44	0.0	0.0	–
15	34	0.56	0.0	0.0	–
16	35	−1.33	0.8	5.4	*Cu, As, Ci*
17	36	0.34	7.0	7.0	*Sc*
18	38	−0.03	7.2	7.4	*Cb, Ac*
19	40	−0.66	1.2	4.0	*Cb, Ac*
20	41	2.87	2.6	6.8	*Ac, Cs*

* According to the day number presented in the Wangara experiment data.

Table 4 Comparison of h_{obs} with h_{MJM}, h_{JM}, and h_{HOL}. The Wangara experiment data are used (20 days, 40 cases).

	$\overline{y}$ (m)	$\overline{x}$ (m)	RMSE (m)	RMSE/$\overline{y}$	r
h_{MJM}	931	942	190	0.204	0.880
h_{JM}	931	916	245	0.263	0.806
h_{HOL}	931	1,322	538	0.578	0.476

Notes;

$\overline{y}$	mean of observed values
$\overline{x}$	mean of calculated values
RMSE	root mean square error; $[\overline{(x-y)^2}]^{1/2}$
r	correlation coefficient

2.2 Estimation of surface flux

2.2.1 Surface heat flux

Simple forms of the equation for latent heat flux LE in terms of net radiation Rn and soil heat flux G were suggested by Priesley and Taylor (1972), *i.e.*,

$$LE = \frac{\alpha}{1 + (\lambda/s)} (Rn - G), \tag{8}$$

where α is a parameter which depends on the soil moisture condition, s defined as $\partial q_s/\partial T$ at appropriate temperature T, q_s the saturation specific humidity, and λ the psychrometric constant.

De Bruin and Holtslag (1982) modified Eq. (8) by adding a constant term b as follows.

$$LE = \frac{\alpha'}{1 + (\lambda/s)} (Rn - G) + b. \tag{9}$$

The energy balance equation for the ground surface is given by

$$Rn = H + LE + G. \tag{10}$$

Using Eq. (10), the corresponding part of Eq. (9) for H is expressed as

$$H = \frac{\alpha'' + (\lambda/s)}{1 + (\lambda/s)} (Rn - G) - b, \tag{11}$$

where $\alpha'' = 1 - \alpha'$.

Holtslag and Van Ulden (1983) showed good agreement between observed H and estimated H using Eq. (11) with $\alpha''=0$, $b=20$ W/m^2 in the Netherlands throughout the year.

At Tsukuba, the soil moisture varies considerably. Therefore Eq. (11) can not be applied directly for this study using a constant value of α'' throughout the year. To derive a empirical equation, which can be used to estimate H based only on routine meteorological data, we modify the scheme previously proposed by De Bruin and Holtslag (1982).

Since there is no routine observation data of soil moisture, a simple parameterization is necessary to determine α''. From Eq. (9), α'' is rewritten as

$$\alpha'' = 1 - \frac{1 + (\lambda/s)}{(Rn - G)} (LE - b). \tag{12}$$

To investigate the seasonal variation pattern of α'', monthly average values of α'' were calculated by Eq. (12) with the evapotranspiration data which were observed with the lysimeter at the Environmental Research Center (ERC), the University of Tsukuba in 1978. Supplimentary data, Rn and air temperature, were taken from routine observation data at the Tateno Aerological Station, located about 8 km south of ERC. Data used in the calculation were monthly average values for daytime situations. Following Holtslag and Van Ulden (1983), G is simply assumed to be 10% of Rn in the present study, and the value of b is taken as 20 W/m^2 in the calculation.

It can be seen that α'' has a pronounced seasonal variation (Table 5). The correlation coefficient between α'' and λ/s is 0.94 (Fig. 5). Thus, α'' can be expressed as

$$\alpha'' = c_1 + c_2(\lambda/s) + B, \tag{13}$$

where c_1 and c_2 are constants, and B represents the diurnal variation term.

Table 5 Comparison between monthly mean α'' and λ/s. Values of Rn, LE, and T used for calculation of α'' and λ/s are monthly mean values for daytime. Units of Rn and LE are W/m^2, and unit of T is °C.

Month	T	Rn	LE	λ/s	α''
JAN.	4.6	155	47	1.07	0.60
FEB.	5.7	169	54	0.97	0.56
MAR.	9.5	235	92	0.82	0.38
APR.	14.9	286	125	0.60	0.35
MAY	18.0	320	154	0.51	0.30
JUN.	20.2	244	162	0.43	0.08
JUL.	26.8	336	223	0.32	0.11
AUG.	26.6	324	195	0.33	0.20
SEP.	21.8	250	156	0.41	0.15
OCT.	17.7	201	96	0.52	0.36
NOV.	10.1	127	55	0.79	0.45
DEC.	7.3	112	44	0.93	0.54

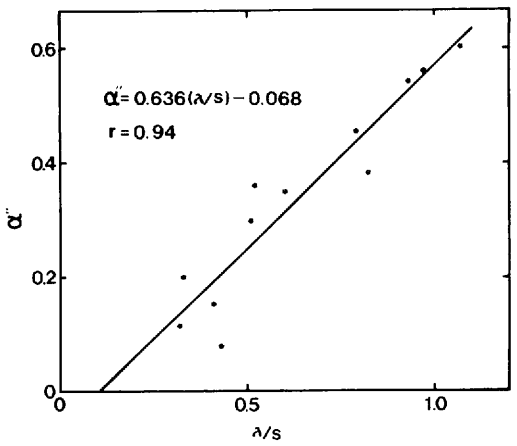

Fig. 5 Relationship between λ/s and α''.

It is interesting to note that De Bruin and Keijman (1979) showed seasonal variation and diurnal variation of α in Eq. (8) by analysis of evaporation data from a shallow lake. Yu (1977) also showed diurnal variation of α, applying the Wangara experiment data.

One reason for diurnal variation of α may be considered as follows; after the sun rises, Rn increases and the temperature gradually becomes higher. In accordance, evapotranspiration also increases. However since the ground surface becomes drier, the increasing rate of evapotranspiration is slower than that of Rn. As a result, α decreases with time. It may be assumed that the minimum value of α occurs at sunrise and maximum at sunset.

From the above considerations, B in Eq. (13) can be simply expressed as a function of time, *i.e.*,

$$B = A \sin \tau, \tag{14}$$

where $\tau=(t-t_r)\pi/t_d - \pi/2$, A the amplitude of B, t_r the time of sunrise, and t_d the length of daytime. Simply, t_r and t_d can be obtained from

$$t_r = p \cos(\frac{d}{365} 2\pi) + q \tag{15}$$

$$t_d = 2(t_t - t_r), \tag{16}$$

where d is number of days counted from the winter solstice, t_t transit time of the sun, p the amplitude of variation of sunrise time throughout a year, q the time of sunrise at the vernal equinox. At Tsukuba, p is about 1.2 hours and q is 05:40 LST.

Tsukuba, belonging to the monsoon region, has a dry and cold climate in the winter season and is wet and hot in summer. Thus, it is considered that A may be propotional to λ/s, *i.e.*,

$$A = c_3(\lambda/s), \tag{17}$$

where c_3 is constant.

Finally, including seasonal and diurnal variation, α'' can be expressed as

$$\alpha'' = c_1 + c_2(\lambda/s) + c_3(\lambda/s) \sin \tau. \tag{18}$$

Substituting Eq. (18) to (11), an empirical formula for H is obtained as

$$H = \frac{c_1 + (1 + c_2 + c_3 \sin \tau)(\lambda/s)}{1 + (\lambda/s)}(Rn - G) - b, \tag{19}$$

where c_1, c_2, c_3 and b are constants which must be determined empirically. Since τ can be calculated with t_r, H can be estimated by Eq. (19) using Rn, G, and temperature.

2.2.2 Friction velocity and Monin-Obukhov length

According to the Monin-Obukhov similarity theory, the nondimensional wind gradient function ϕ_m is expressed as

$$\phi_m = \frac{kz}{u_*}\frac{\partial u}{\partial z}, \tag{20}$$

where k is the von Karman constant usually given as 0.4, z the height, u the mean wind speed, and u_* the friction velocity.

Several empirical formula have been suggested to describe the relationship between ϕ_m and Monin-Obukhov length L. Observations over uniform terrain in unstable condition obey an equation of the form (Businger *et al.*, 1971)

$$\phi_m = [1 - 16(z/L)]^{-1/4}, \tag{21}$$

where z/L is the stability parameter in the surface layer.

An integrated form of ϕ_m which is useful for wind profile calculation was solved by Paulson (1970). For unstable conditions, the stability function ψ_m is expressed as

$$\psi_m = \int \frac{z/L}{z_0/L} [1 - \phi_m(\zeta)] \frac{d\zeta}{\zeta}$$

$$= 2 \ln(\frac{1 + x}{2}) + \ln(\frac{1 + x^2}{2}) - 2 \tan^{-1} x + \frac{\pi}{2}, \tag{22}$$

where z_0 is the roughness length, $\zeta = z/L$, x and L are

$$x = [1 - 16(z/L)]^{1/4} \tag{23}$$

$$L = -\frac{\rho c_p T u_*^3}{kgH}. \tag{24}$$

Using ψ_m and wind speed u_z at height z, u_* is written as

$$u_* = \frac{ku_z}{\ln(z/z_0) - \psi_m(z/L)} \quad . \tag{25}$$

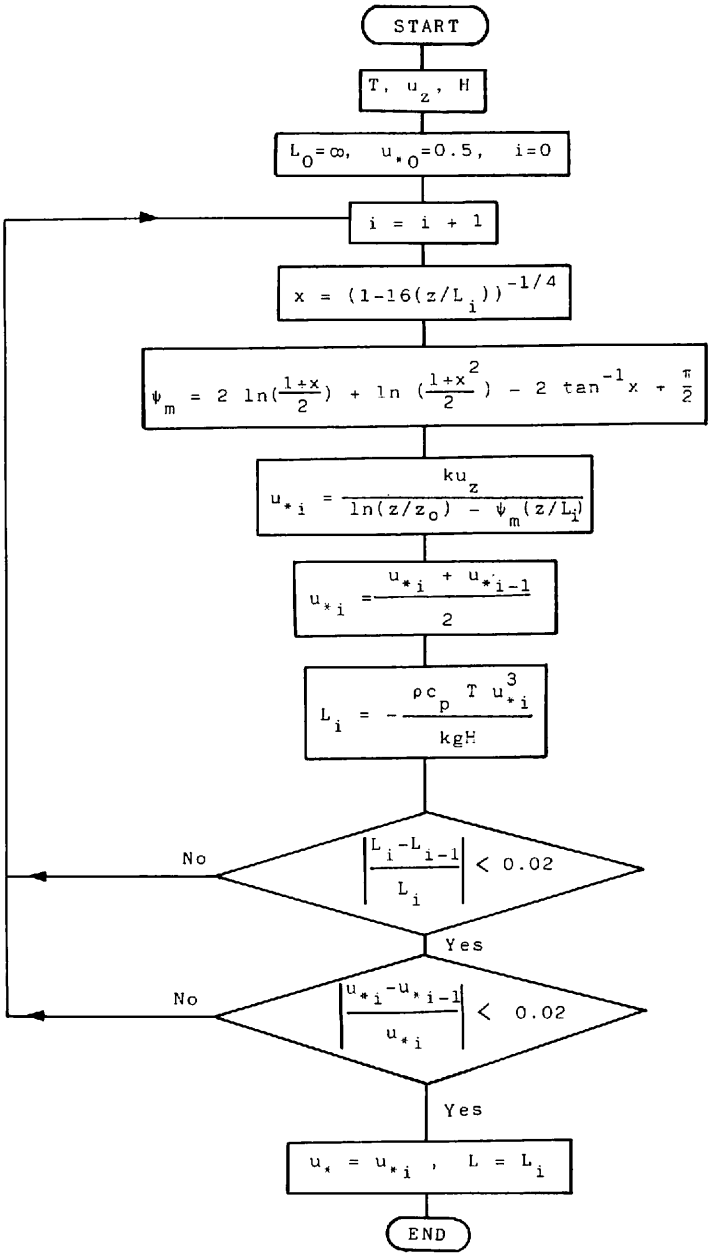

Fig. 6 Flow chart of the estimation scheme for u_* and L.

From Eqs. (22), (23), (24), and (25), L and u_* can be solved by iteration when T, H, z_0, and u_z are known. In order to estimate u_* and L, the procedure described below is used.

Initially we assume the stability as neutral, put $L=\infty$, and u_* as 0.5 m/s. Then, u_* can be computed by Eqs. (22) and (25) with wind speed data. Newly obtained u_* and the previous u_* are averaged. L is computed by Eq. (24) using the average u_* and data of T and H. Then, L is substitued into Eq. (23). By use of Eqs. (22) and (25), the improved value of u_* is obtained. This cycle is repeated until the successive values of L and u_* do not change by more than 2%.

It appears that only a few cycles, usually no more than 10, are needed in order to achieve the required accuracy for u_* and L.

In order to avoid a divergence of solution, it is necessary to substitute averaged values of successive u_* in Eq. (24). A flow chart of this scheme is shown in Fig. 6.

Data required for the application of the scheme are wind speed and temperature at a single height and H, which can be estimated by Eq. (19).

2.3 Turbulence terms

We consider estimation schemes for turbulence characteristics of the convective boundary layer.

Standard deviations of vertical velocity in the unstable surface layer are a function of stability. Following Panofsky *et al.* (1977), it is given that

$$\frac{\sigma_{ws}}{u_*} = 1.25[1 - 3(z/L)]^{1/3} , \tag{26}$$

where σ_{ws} is the standard deviation of vertical velocity in the surface layer. For temperature

$$\frac{\sigma_{Ts}}{T_*} = D(-z/L)^{-1/3} , \tag{27}$$

where σ_{Ts} is the standard deviation of temperature in the surface layer, D a constant, and T_* the scaling temperature in the surface layer, defined by

$$T_* = -\frac{\overline{(w'\theta')}}{u_*} . \tag{28}$$

Using the Kansas data, D was found to be -0.95 by Wyngarrd *et al.* (1977).

Above the surface layer, variances are related to z/z_i, where z_i is the height of the inversion base which is identical to h for the unstable case. We postulate the standard deviation of vertical velocity in the convective boundary layer σ_{wb} as

$$\frac{\sigma_{wb}}{w_*} = f(z/z_i) , \tag{29}$$

where w_* is the scaling velocity in the planetary boundary layer, defined by

$$w_* = \left(\frac{gHz_i}{\rho c_p T}\right)^{1/3} . \tag{30}$$

At present, the function $f(z/z_i)$ is not well known. However from the results of Caughey and Palmer (1979), it is known that $f(z/z_i)$ is almost constant, about 0.57, between the height of about $0.2z_i$ and $0.8z_i$.

Standard deviation of temperature in the boundary layer σ_{Tb} is also a function of z/z_i. For the free convection case it can be written as (Caughey and Palmer, 1979)

$$\left(\frac{\sigma_{Tb}}{\theta_*}\right)^2 = 1.8(z/z_i)^{-2/3} , \tag{31}$$

where θ_* is the scaling temperature in the boundary layer, defined by

$$\theta_* = \frac{\overline{(w'\theta')}}{w_*} . \tag{32}$$

Eq. (31) fits well up to $0.8z_i$.

Vertical exchange coefficients depend on many variables such as height above the ground, roughness of the surface, wind speed, and hydrostatic stability. Here we consider the exchange coefficient for momentum K_m and for heat K_h.

Definition of K_m is momentum flux per local wind gradient. It is written as

$$K_m = -\frac{\overline{(w'u')}}{\partial u/\partial z} , \tag{33}$$

where $\overline{(w'u')}$ is $-u_*^2$. When wind profile data are not available, using Eq. (20), Eq. (33) is written as

$$K_m = \frac{ku_*z}{\phi_m} . \tag{34}$$

Similar to momentum, K_h is expressed as

$$K_h = -\frac{\overline{(w'\theta')}}{\partial\theta/\partial z} , \tag{35}$$

where $\partial\theta/\partial z$ in the surface layer is expressed as

$$\frac{\partial\theta}{\partial z} = \frac{T_*}{kz}\phi_h , \tag{36}$$

where ϕ_h is the nondimensional temperature gradient function. It can be written as

$$\phi_h = [1 - 16(z/L)]^{-1/2} . \tag{37}$$

From Eqs. (35), (36) and (28), K_h is written as

$$K_h = \frac{ku_* z}{\phi_h} \tag{38}$$

or

$$K_h = \frac{ku_* z}{\phi_m{}^2} . \tag{39}$$

Using Eqs. (34) and (39), K_m and K_h can be obtained from the data of H, u_*, and temperature.

At higher levels, the sign of the flux is not determined by the local gradient, because direction of gradient of potential temperature or wind speed, and direction of heat or momentum flux are not always identical. Thus Eqs. (33) and (35) become meaningless. In the present study, we consider the exchange coefficients in the surface layer only.

CHAPTER III

EVALUATION OF CONVECTIVE BOUNDARY LAYER MODEL WITH FIELD OBSERVATION AT TSUKUBA

3.1 Details of field observation

Observation of the boundary layer was carried out at the Meteorological Research Institute (MRI; 36.03 N, 140.08 E) in Tsukuba Academic New Town, Japan. Tower observation was performed during the period from December 1982 to February 1984, and 24 soundings were obtained from low level sonde observations during the observation period.

The observation site is near the center of the Kanto Plain, Excluding Mt. Tsukuba (20 km north from MRI, height 876 m), there is no mountainous area higher than 100 m within 50 km (Fig. 7)

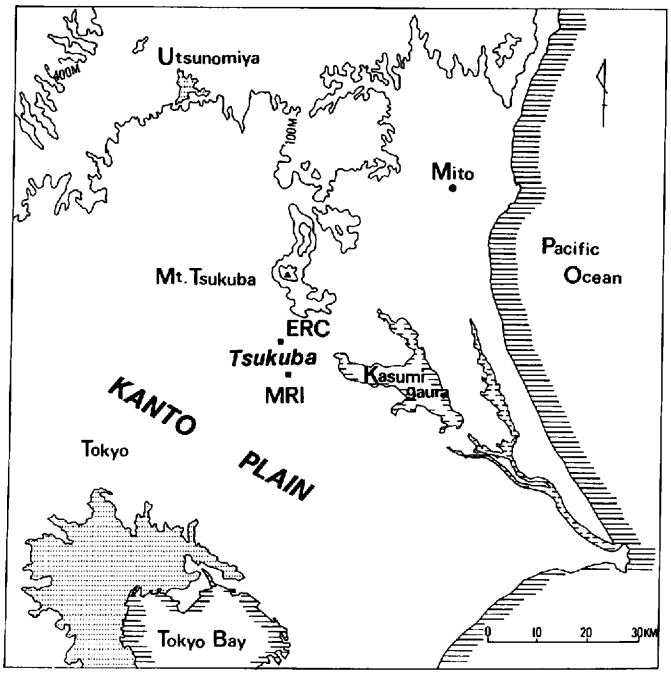

Fig. 7 Map of the observation site and surroundings.

Lake Kasumigaura (area 168 km^2, maximum depth 7 m) is located 15 km east of MRI. The distance from the observation site to the nearest sea shore is about 45 km. Since the nearest sea shore is located adequately far away from the observation site, and Lake Kasumigaura is not so deep as to generate a sufficient lake breeze, in the present study, effects of sea breeze and lake breeze are ignored.

The observation site is composed of flat terrain with scattered forest, dominated by pine trees. At the site, z_0 is about 0.4 m (Naito *et al.*, 1983).

In order to observe the meteorological quantities in the surface layer and in the lower part of the boundary layer, the 213 m meteorological tower at MRI was used. Observation levels of the tower are 10 m, 25 m, 50 m, 100 m, 150 m, and 200 m. A sonic anemometer thermometer, platinum thermometer, capacitance hygrometer, and propeller anemometer are installed at every level. The observation items are temperature, wind speed, variances of temperature and wind speed component, heat flux, and momentum flux (Table 6). The details of observation systems of the tower were given by Hanafusa *et al.* (1979).

Table 6 Brief description of meteorological elements and instruments of the observation performed using the 213 m meteorological tower at the Meteorological Research Institute.

Element	Instrument
Mean temperature	Pt resistant-thermometer
Mean wind speed	propeller anemometer
Fluctuation of wind and temperature	Sonic anemometer-thermometer
Heat and momentum flux by eddy correlation method	Sonic anemometer-thermometer

For the present study, from the tower data, hourly values observed between 08:00 and 16:00 LST at the 25 m level were used. The cases of precipitaiton and strong wind, wind speeds exceeding 7 m/s, were excluded. Finally, 191 sets of hourly data were analyzed. The period of the observation is shown in Table 7.

Table 7 Period of the tower observation.

No.	Period
1	15 Dec. 1982 – 10 Jan. 1983
2	25 Jan. 1983 – 9 Feb. 1983
3	28 Jul. 1983 – 9 Aug. 1983
4	9 Nov. 1983 – 18 Nov. 1983
5	15 Feb. 1984 – 17 Feb. 1984

In order to obtain potential temperature profiles, the low level sonde observation was carried out (Table 8). Air temperature, wet bulb temperature, and pressure were observed up to 3 km with low level sonde, supplied by Meisei Electric Co..

Supplemental data for analysis were hourly Rn and routine sonde data, which were observed at the Tateno Aerological Station about 300 m away from the observation site. The values of w_h

Table 8 Summary of low level sonde observation.

Date	Weather condition	Start time (LST)	Run no.
28 Jul. 1983	scatter, *Cu* increased in the afternoon	10:37	1
		13:30	2
		15:06	3
29 Jul. 1983	scatter	10:05	4
		11:40	5
		13:50	6
		15:24	7
3 Aug. 1983	scatter	11:00	8
		13:00	9
		14:39	10
4 Aug. 1983	scatter	10:33	11
		12:44	12
		14:30	13
9 Nov. 1983	scatter	11:45	14
16 Nov. 1983	clear	12:00	15
		14:33	16
17 Nov. 1983	scatter, wind speed increased in the afternoon	14:43	17
15 Feb. 1984	scatter	12:01	18
		13:44	19
		14:20	20
16 Feb. 1984	scatter, wind speed increased in the afternoon	10:20	21
		13:20	22
17 Feb. 1984	overcast	10:20	23
		11:20	24

were obtained from the data of initial conditions of the numerical model used for routine weather forcasting by the Japan Meteorological Agency (Meteorological Research Institute, 1983). In the numerical model, w_h is determined from the data of the radiosonde net work. In the present study, w_h for 800 mb or 850 mb at the nearest mesh to Tsukuba are used.

Temperature and wind speed were observed at one hour intervals at the tower. However since Rn and the other values observed at the tower were recorded during every hour, a descre pancy arises when analyzing by use of such data set in computation. To make the data set agree in a time scale, temperature and wind speed data of successive times were averaged. We consider that these data represent values between successive times. For example, in Chapter IV the averaged value for temperatures at 08:00 and 09:00 LST and Rn, which occurred during the period between 08:00 and 09:00 LST, will be regarded to represented the values at 08:30 LST.

3.2 Empirical equation of surface heat flux

Coefficients in Eq. (19) were determined by the multiple regression method, using hourly values of observed H, Rn, and temperature for 8 hours in the daytime; 08:00 – 16:00 LST. Although the spring season was not included in the data set, we believe that these data properly include various conditions throughout a year.

The empirical equation of H determined by these data is as follows.

$$H = \frac{-0.01 + (1.67 + 0.55 \sin\tau)(\lambda/s)}{1 + (\lambda/s)} (Rn - G) - 15.2 , \qquad (40)$$

where units of H, Rn, and G are W/m^2.

Since a limited number of observed data are available, Eq. (40) is evaluated with the data which are the same data used to determine the coefficients in this equation. However it may be considered that the result of evaluation is not so different compared to evaluation with another data set, because the data set used to determine the coefficients of empirical equation is considered properly to cover the conditions of a whole year.

Fig. 8 exhibits comparison between observed heat flux H_{obs} and estimated heat flux H_{est}. RMSE of H_{est} is 24 W/m^2, which corresponds to about 25% of the mean value of H_{obs}. Fig. 9 shows a comparison between the daytime mean H_{est} and that of H_{obs}. RMSE of the daytime mean value is 14 W/m^2, which corresponds to 14% of the mean value of H_{obs}.

Application of this type of empirical equation is restricted to daytime conditions only, and should not be applied to regions where the seasonal variation pattern of soil moisture condition is not closely related to seasonal variation pattern of air temperature.

Since the empirical equation requires only hourly data of Rn and temperature, it is suitable for practical use in estimation of H.

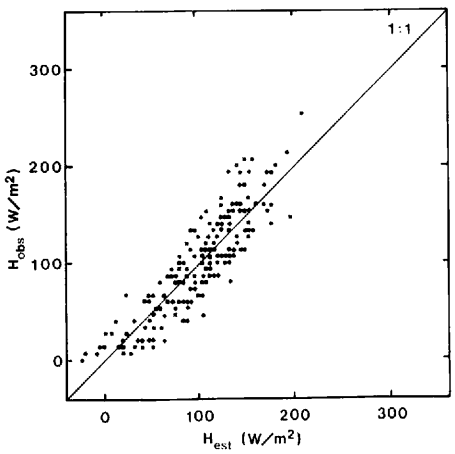

Fig. 8 Comparison of H_{obs} with H_{est} according to Eq. (40).

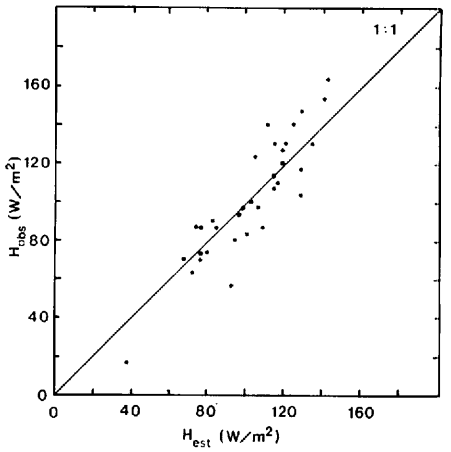

Fig. 9 Comparison of daytime mean value of H_{obs} with that of H_{est}.

3.3 Evaluations of estimation scheme of friction velocity and Monin-Obukhov length

A scheme, which estimates u_* and L, is evaluated with hourly data observed at the tower. Observed Monin-Obukhov length L_{obs} is calculated by Eq. (24) with observed data of u_*, H, and temperature.

Estimated friction velocity u_{*est} and estimated Monin-Obukhov length L_{est} are calculated

by the scheme described in 2.2.2. The wind speed and H observed at 25 m level of the tower are used in the calculation.

A comparison between observed friction velocity u_{*obs} and u_{*est} shows fairly good agreement (Fig. 10). RMSE of u_{*est}, compared to u_{*obs}, is 0.072 m/s as seen in Table 9. In Fig. 11, L_{est} do not fit observed values as well as in the case of u_* (Table 9). Since L is proportional to ${u_*}^3$, any error in u_* is exaggerated.

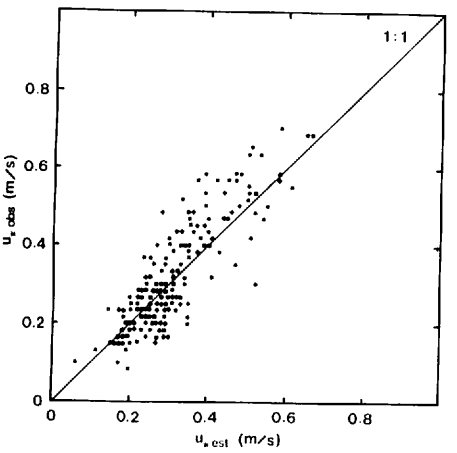

Fig. 10 Comparison of u_{*obs} with u_{*est} according to the scheme described in 2.2.2.

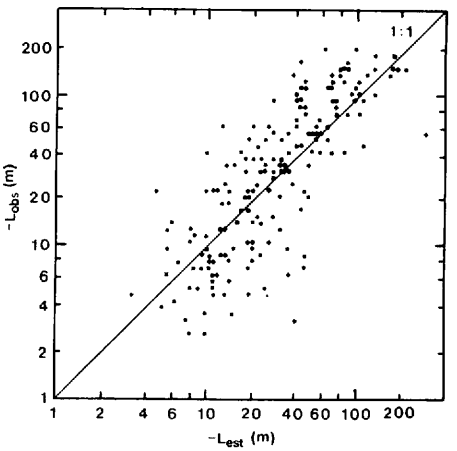

Fig. 11 Same as Fig. 10, but for L.

Table 9 Comparison of estimated values with observed values for u_* and L. Units of u_* is m/s and unit of L is m. *See* notes in Table 4.

	$\bar{y}$	$\bar{x}$	RMSE	RMSE/$\bar{y}$	r
u_*	0.325	0.313	0.072	0.222	0.856
$-L$	53.5	43.5	38.5	0.720	0.718

3.4 Evaluation of mixed layer height model

In 2.1.3, the evaluation of the MJM using the Wangara experiment data showed that the modification of the jump model improves results. However, in order to apply the MJM to Tsukuba, it is desirable to evaluate the MJM with data that has been observed at Tsukuba.

The MJM is evaluated with observed h, which is determined as being the height of the lowest potential temperature inversion layer base. Twenty four soundings by use of the low level sonde are used in the analysis.

Initial conditions, such as h_0, $\Delta\theta_0$, γ_0, required in the MJM were taken from radiosonde data observed at 08:30 LST at the Tateno Aerological Station. For H and u_*, hourly values observed at the tower by the eddy correlation method were used, and linearly interpolated to obtain values at

intermediate times. For each day, the calculation was carried out for 7 hours starting at 08:30 LST.

Examples of development of the mixed layer are presented for the case when thermal convection prevailed (Fig. 12), and prevalence of mechanical convection (Fig. 13). The solid line represents h_{MJM}, the dashed line represents h calculated by the jump model, h_{JM}, and circles represent the observed values, h_{obs}. For the case of thermal convection, h_{MJM} is similar to h_{JM}. However, for the case of mechanical convection, the difference becomes large as u_* increases. It is clear that in the case of Fig. 13, the role of mechanical convection is important in the development of the mixed layer, and thus, the result is improved by modification of the jump model.

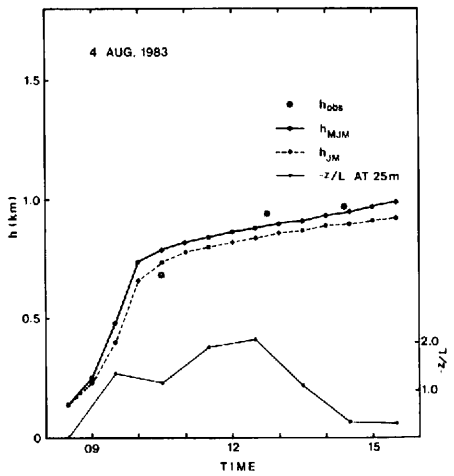

Fig. 12 Development of the mixed layer under convective condition.

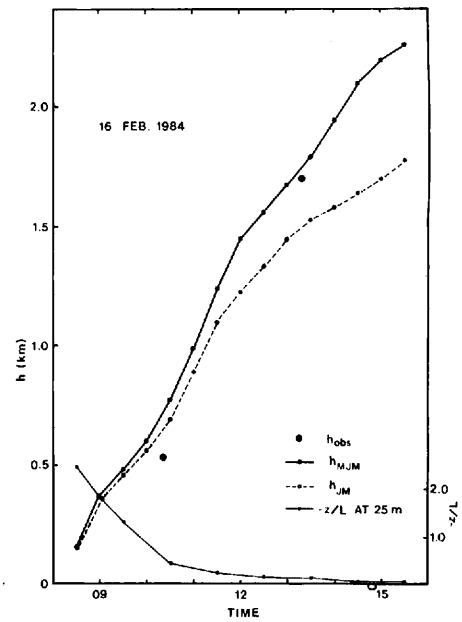

Fig. 13 Same as Fig. 12, but for the case of mechanical convection.

Fig. 14 shows comparisons between h_{MJM} and h_{obs} for 24 cases. RMSE of h_{MJM} is 102 m as shown in Table 10. This corresponds to about 12% of the mean value of h_{obs}. On the other hand, RMSE for h_{JM} is 195 m. For the Wangara experiment data, RMSE is somewhat large compared to the case of Tsukuba. It is considered that one of the reasons is presumably due to the error which is incurred in the estimation of H by the flux-profile method. It is clear that the modification of the jump model for the mechanical convection term and large scale vertical motion improves results.

The MJM itself contains error. However, when one estimates h using the MJM with estimated H and u_* as input data, results are affected by the error of these input data. It is considered that the estimation error of h increases somewhat.

In the calculation of h, an integrated value of H during the desired time is important. RMSE of hourly H is about 25%, however RMSE of mean H during the daytime decreases to 14%. Since

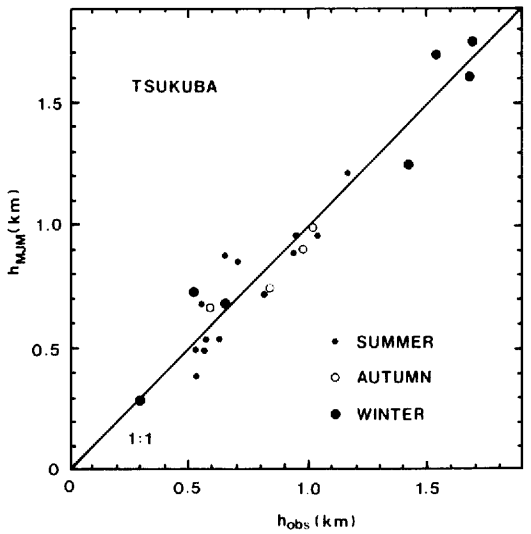

Fig. 14 Comparison between h_{obs} and h_{MJM} using the data observed at Tsukuba.

Table 10 Comparison of h_{obs} with h_{MJM}, h_{JM}, and h_{HOL}. Data of 24 cases at Tsukuba are used. *See* notes in Table 4.

	$\bar{y}$ (m)	$\bar{x}$ (m)	RMSE (m)	RMSE/$\bar{y}$	r
h_{MJM}	872	859	102	0.117	0.966
h_{JM}	872	760	195	0.224	0.910
h_{HOL}	872	1,337	624	0.716	0.662

h is roughly propotional to the square root of H, in the calculation of h, an error of about 7% may by introduced due to the error in estimation of H.

RMSE of u_* is 0.072 m/s (Table 9). From the result of the sensitivity test in 2.1.2, it is considered that this range of error affects h only a small percent.

In Table 10, h determined by Holtzworth's scheme, h_{HOL}, are listed together. Generally, h_{HOL} is remarkably higher than h_{MJM}. One of the reasons for this is presumably due to the effect of the super adiabatic layer near the surface being included in Holzworth's scheme.

Based on the results of the above evaluation, it can be judged that the MJM is suitable for estimating h.

3.5 Standard deviations of vertical velocity and temperature

The standard deviations of vertical velocity and temperature in the surface layer are estimated by Eqs. (26) and (27) respectively for 25 m level. The data required in the calculation are obtained from the tower.

Estimated σ_{ws} and σ_{Ts} agree fairly well with observed values (Figs. 15 and 16). However, there is a trend for observed values to be slightly smaller than estimated values. This trend may possibly be explained as follows:

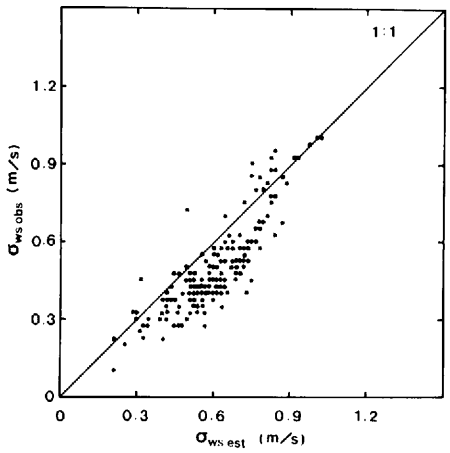

Fig. 15 Comparison of observed σ_{ws} (σ_{wsobs}) with the estimated values (σ_{wsest}) by Eq. (26).

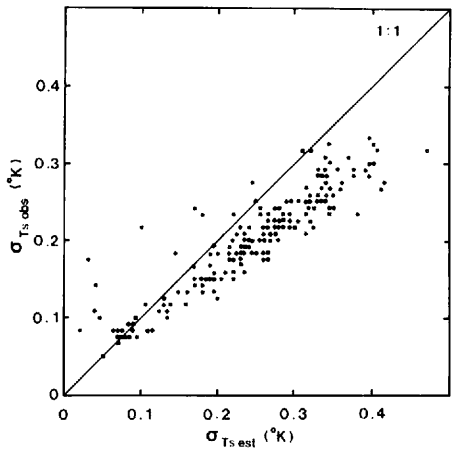

Fig. 16 Comparison of observed σ_{Ts} (σ_{Tsobs}) with the estimated values (σ_{Tsest}) by Eq. (27).

Since the averaging time adopted for this study is 10 minutes, which may be somewhat short to include the variance of low frequency, observed σ_{Ts} and σ_{ws} may fail to include values occurring at a low frequency (Hanafusa, personal communication).

RMSE of σ_{wsest} is 0.142 m/s which corresponds to 29% of the mean observed value, and RMSE of σ_{Tsest} is 0.062°K which corresponds to 31% of the mean observed value (Table 11).

Table 11 Comparison between observed values and estimated values for σ_{ws} and σ_{Ts}. Units of σ_{ws} and σ_{Ts} are m/s and °K respectively. *See* notes in Table 4.

	$\bar{y}$	$\bar{x}$	RMSE	RMSE/$\bar{y}$	r
σ_{ws}	0.497	0.608	0.142	0.286	0.856
σ_{Ts}	0.200	0.244	0.062	0.310	0.914

In the present study, Eqs. (29) and (31) which can be used to estimate σ_{wb} and σ_{Tb}, could not be evaluated with observed values, because the tower, height of 213 m, is not sufficiently high to obtain the variances in the boundary layer.

3.6 Discussions on accuracy of the model applied to climatological study of convective boundary layer

In Chapter II, we have constructed a model with which the structure of the convective boundary layer is obtained. The model requires only routine meteorological observation data. Therefore, the model can be applied to climatological study of the convective boundary layer.

In this section, we discuss the accuracy of the model when it is applied to climatological study of the convective boundary layer. Two types of errors arise in the calculation of the model, *i.e.*, random error and systematic error. Random error arises due to inaccuracy of input data and partly due to physical processes which are not well known.

In order to investigate the seasonal and diurnal variation of the convective boundary layer, we will use monthly mean or percentile values in Chapter IV. In this case, random error is canceled by averaging. Thus systematic error, which remains after averaging, is important.

Systematic error can be detectable from a trend line in the scatter diagram. However, for simplicity, we regard the difference between the mean observed value and the mean estimated value as systematic error.

Although systematic error of the empirical equation of H could not be detected by evaluation in Section 3.2, it is considered that systematic error of the estimated H by Eq. (40) may be sufficiently small. As seen in Table 9, systematic error of u_* is 0.012 m/s and this corresponds to only 4% of the mean observed u_*. For L, systematic error is 10.0, corresponding to 19% of the mean observed value.

Systematic error of h is related not only to error of the MJM itself, but error of input data such as H and u_*. However, since systematic error of estimated H and estimated u_* are sufficiently small, if we ignore this error, systematic error of h may be 13 m, corresponding to 2% of the mean observed h.

From results in section 3.5, systematic errors of σ_{ws} and σ_{Ts} are 0.111 m/s and 0.044°K/s, respectively. Since observation of the variances include problems as described in Section 3.5, it is considered that systematic errors of these values decrease more or less in actual cases.

There are no data to evaluate equations for w_*, σ_{wb}, σ_{Tb}, K_m, and K_h. However, since these values are proportional to linear or, 1/3 or 1/4 power of values, such as H, u_*, and h, it is considered that systematic errors of these values are sufficiently small.

Accuracy of the model discussed above is valid under the assumption of the Monin-Obukhov similarity theory.

CHAPTER IV

CLIMATOLOGICAL ASPECTS OF CONVECTIVE BOUNDARY LAYER

4.1 Methods

Climatological aspects of the convective boundary layer are investigated over a 3 year period, Founamental values in the surface layer such as H, u_*, and L are estimated. Using these values, h and characteristic parameters of turbulence are obtained.

The calculations are carried out by following the steps listed below.

(1) Using hourly data of Rn and temperature, H is estimated by Eq. (40).

(2) With the scheme described in 2.2.2, u_* and L are obtained. Data required in the scheme are estimated H in (1) and wind speed.

(3) Using the MJM, h is calculated. Input data are H, and u_* estimated in (1) and (2), initial profile of potential temperature, and w_h. Intermediate values of H and u_* between successive hourly values are obtained by linear interpolation.

It is difficult to determine h_0 and $\Delta\theta_0$ with the potential temperature profile obtained from radiosonde data. However as shown in 2.1.2, results become insensitive to these initial conditions within about one hour. Therefore, in practical calculations for climatological study, h_0 and $\Delta\theta_0$ are simply assumed as 50 m and 0.5°C respectively.

(4) Using Eq. (30), w_* is calculated with H estimated in (1), h calculated in (3), and observed temperature data.

(5) From the data estimated in (2) and (3), z/L and h/L are obtained.

(6) Using Eqs. (26), (27), (29), and (31), σ_{ws}, σ_{Ts}, σ_{wb}, and σ_{Tb} are calculated with the data obtained in the above steps.

(7) Values of K_m and K_h are calculated by Eqs. (34) and (39) with u_* and L being determined in (2).

In the above steps, surface layer quantities are calculated for 25 m level, and quantities in the boundary layer are obtained for the level of $h/2$.

The schemes described above are theoretically valid for unstable atmospheric conditions only. Thus, calculations are carried out from 08:30 to 16:00 LST for each day.

In order to investigate the diurnal and seasonal variations of the convective boundary layer, we use monthly values for each hour.

It was found from preanalysis of hourly values calculated by steps (1) – (7), that distributions were skewed and abnormal for a significant number of monthly data sets. Therefore, in order to avoid the effects of singularity and skewness, percentiles are used to represent monthly values, rather than monthly averages.

Turbulent mixing is generated by thermal and mechanical convection. It is also controlled by the potential temperature gradient at the stable layer above the mixed layer. The potential temperature gradient is obtained from 08:30 LST sounding for each day. Here we use the averaged value between 500 m and 1,500 m; $\gamma_{500\text{-}1500}$. At the lower part of the boundary layer, the potential temperature gradient varies considerably according to the stages of distruction of the

surface inversion. At the 08:30 LST sounding, the stages are quite difference by season because of varying sunrise time. Thus, to compare the representative values of the potential temperature gradient, we take 500 m as the lower boundary for averaging the potential temperature gradient instead of the surface. The scheme to determine $\gamma_{500\text{-}1500}$ is explained in Fig. 17.

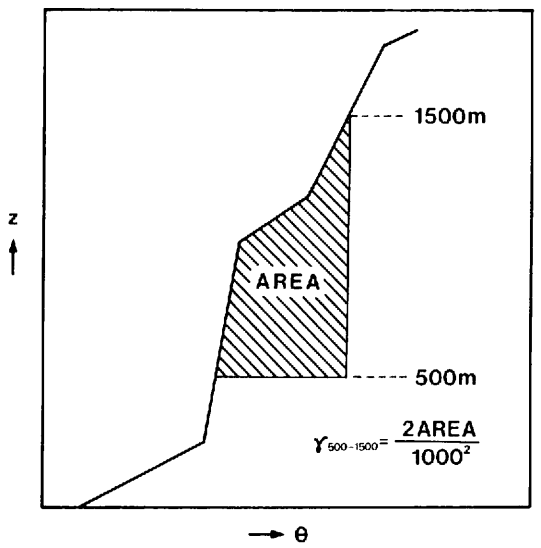

Fig. 17 The scheme of determination of $\gamma_{500\text{-}1500}$. First, the area is derived from the potential temperature profile, then this value substitute to inserted equation to obtain $\gamma_{500\text{-}1500}$.

We investigate the relationship between the development of the mixed layer and vertical profile of the potential temperature gradient. Since observation heights of radiosonde are different for each sounding, to obtain the mean profile of the potential temperature gradient, we adopt the following procedure.

(1) The potential temperatures at each 50 m level are obtained by linear interpolation with sounding data.
(2) The potential temperature gradients are calculated for every 50 m.
(3) For each level, the potential temperature gradients are averaged over the desired number of soundings.

The potential temperature gradient varies mainly according to air mass types. Excluding the arctic air mass, air mass types can be divided into four types depending on physical properties of source area (Barry and Perry, 1973). These are continental polar air mass (cP), continental tropical air mass (cT), maritime polar air mass (mP), and maritime tropical air mass (mT).

For the purposes of the present study, it is necessary to identify air masses which influence the weather at Tsukuba area.

When a migratory anticyclone, which is isolated from the continental air mass, moves easterly toward the sea surface, physical properties of the air mass are changed from the lower level. Thus,

the potential temperature profile of a migratory anticyclone becomes different from that of the continental air mass, especially for the lower part of the air mass.

During the break out period in winter, cP which develops on the East Asian continent influences Japan directly through a strong northwesterly wind. However, after the break out period, strength of the cP weakens. The air mass passing over the Sea of Japan is warmed by heating from the sea surface. Therefore, physical properties such as potential temperature change quickly.

Yoshino (1968) and Yoshino and Kai (1974) classified pressure patterns over Japan and its surrounding regions into fifteen types. They showed that occurrence frequency of migratory anticyclone is high in spring and autumn; over 40% in April and October. West-high-east-low

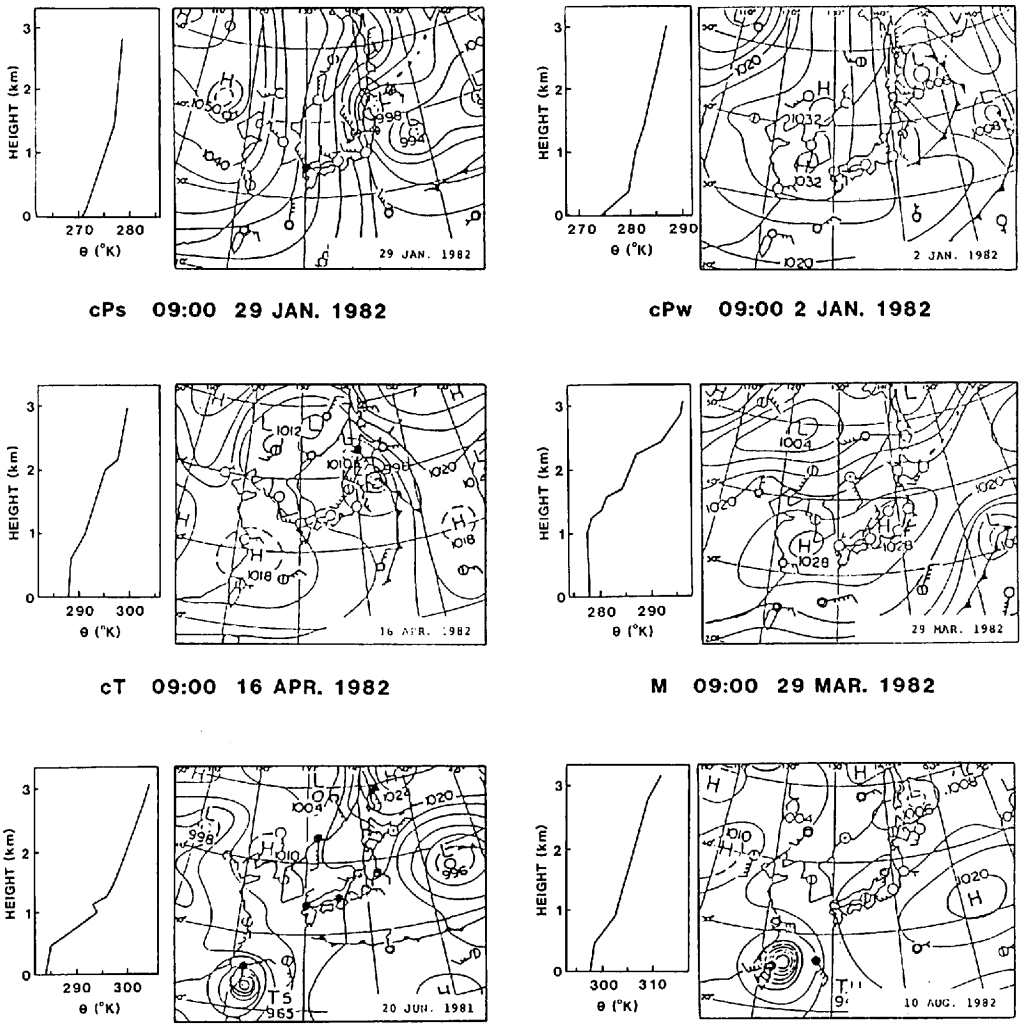

cPs 09:00 29 JAN. 1982 cPw 09:00 2 JAN. 1982

cT 09:00 16 APR. 1982 M 09:00 29 MAR. 1982

mP 09:00 20 JUN. 1981 mT 09:00 10 AUG. 1982

Fig. 18 Typical examples of pressure patterns and potential temperature profiles for the six air mass types.

patterns, which can be regarded as cP type in the present study, are the most frequent in winter; that is over 40% in January.

From the view point of potential temperature profile, the migratory anticyclone type is added to the four primary air mass types, and the cP type is further divided into two types in this study. Finally, air mass types are classified into six types as follows.

(1) cPs ; Strong continental polar air mass.
(2) cPw ; Weak continental polar air mass.
(3) cT ; Continental tropical air mass.
(4) M ; Migratory anticyclone or zonal shape anticyclone
(5) mP ; Maritime polar air mass.
(6) mT ; Maritime tropical air mass.

Low pressure systems, which affect weather at the Tsukuba area, are not considered in the air mass classification, because weather conditions such as precipitation and large amount of low clouds are excluded, as will be described in Section 4.2. Air mass types which influence the Tsukuba area are determined for each day, based on surface weather maps at 09:00 LST. Typical examples of these six types are presented in Fig. 18.

Thermal convection is controlled by insolation which is related mainly to sky conditions. Sky conditions are classified into two cases, i.e., fair weather condition; total cloud amount $< 70\%$, and cloudy condition; total cloud amount $\geqslant 70\%$.

In order to investigate the relationships between parameters in the convective boundary layer and synoptic conditions, results of the calculations are sorted according to air mass types and sky conditions on a monthly basis.

4.2 Data and limitations of weather conditions

For climatological study of the convective boundary layer, air temperature, wind speed, potential temperature profile, and Rn are used. Hourly values of air temperature and wind speed are taken from the tower at the 25 m level. Hourly values of Rn, which were observed at the Tateno Aerological Station, are also used.

The radiosonde observations are carried out routinely twice a day at the Tateno Aerological Station, *i.e.*, 08:30 and 20:30 LST. These data are printed monthly in the Aerological Data of Japan. For the present study, radiosonde soundings at 08:30 LST are used to determine h_0, $\Delta\theta_0$, and γ_0. We obtained the value of w_h from the data of initial conditions of the numerical model used for routine weather forcasting.

To determine the air mass types, surface weather maps at 09:00 LST are used. Sky conditions data are obtained from the weather code in the Aerological Data of Japan.

Since the MJM is limited to weather conditions described in 2.1.1, weather conditions which will be described below were excluded from analysis. In the case of strong wind, there is significant error of entrainment rate due to mechanical convection and horizontal advection. Therefore, in order to avoid these effects, cases in which daytime mean wind speed exceeded 7 m/s, were excluded. Since existance of cloud layer or precipitation could induce diabatic heating by condensation and radiation, cases, when amount of low level cloud was more than 50%, or when precipitation occurred, were also excluded.

After excluding these cases, we use data for 616 days over a three year period (Table 12).

Table 12 Number of days for climatological analysis of the convective boundary layer over 3 years; 1980–1982.

(days)

Month	Fair weather	Cloudy	Total
Jan.	52	14	66
Feb.	51	15	66
Mar.	38	17	55
Apr.	34	18	52
May	35	16	51
Jun.	18	17	35
Jul.	10	18	28
Aug.	17	20	37
Sep.	29	21	50
Oct.	41	17	58
Nov.	37	14	51
Dec.	56	11	67
Annual	418	198	616

4.3 Seasonal variation of structure of convective boundary layer

Among hourly values in the daytime, values at 12:30 LST, when convection is considered to be most active, are selected to study the seasonal variation of structure of the convective boundary layer. However, for surface heat balance terms, mean values during the daytime between 08:00 and 16:00 LST are used, and for h, values at 14:30 LST, near the time when the daily maximum temperature occurs, are used.

In the analysis, to represent the monthly value, we use the median rather than the monthly mean. In order to indicate the range of these values 10, 25, 75 and 90 percentiles are used instead of standard deviation, or minimum and maximum.

Seasonal variations of surface heat balance terms in the daytime are shown in Fig. 19. Where Rn is an observed value, H is estimated by Eq. (40), and LE is deduced from Eq. (10). In December, H is smallest, 77.6 W/m^2, and largest, 170.2 W/m^2, in March. It is relatively small in summer compared to Rn, due to the large amount of evaporation.

The value of u_* varies throughout the year, being smallest in November, 0.26 m/s, and largest in April, 0.43 m/s (Fig. 20). Regarding w_* as the intensity of convection, one can say from Fig. 20 that convection is most intensive in spring.

The seasonal variation of z/L at 25 m and h/L are given in Figs. 21 and 22, respectively. The surface layer is most unstable in November and least unstable in April. In the case of the boundary layer, it is most unstable in March; the median of h/L is -46.4. It is worth noting that in the daytime, stability of the surface layer is most unstable in autumn, and for the boundary layer, most unstable in spring.

The seasonal variation of h shows two peaks (Fig. 23). It is high in spring and low in winter. Maximum and minimum of median values are 1,490 m in March and 816 m in December respec-

tively. Notably, it is not so high in summer, in spite of strong solar radiation. Referring to the 10 and 90 percentiles, it can be pointed out that day to day variation of h is also large in spring and small in summer. This will be discussed in the following section.

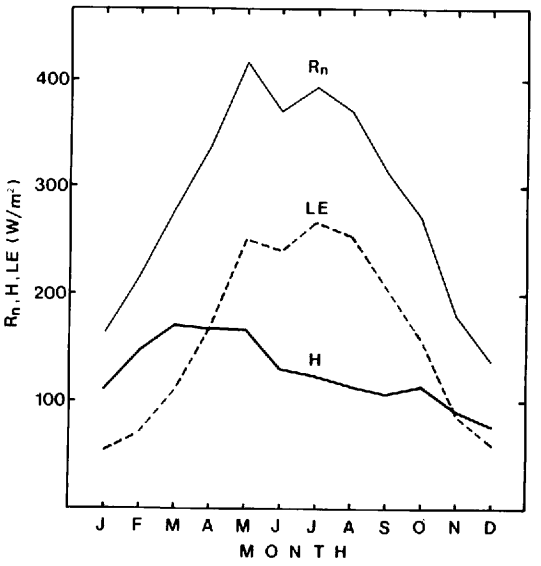

Fig. 19 Seasonal variations of surface heat balance components in daytime.

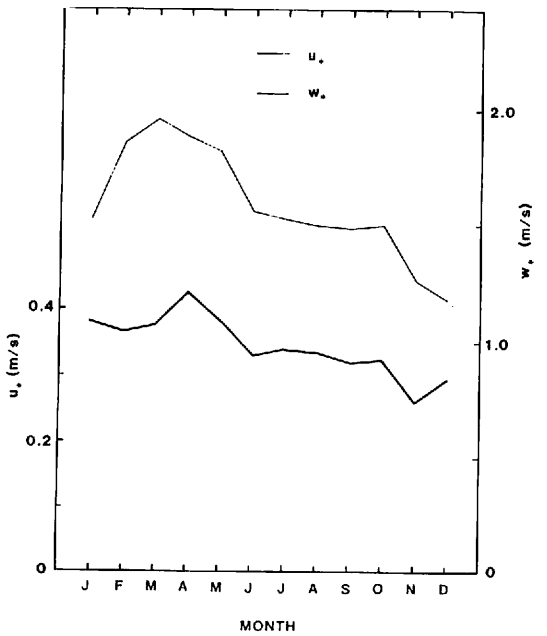

Fig. 20 Seasonal variations of u_* and w_*.

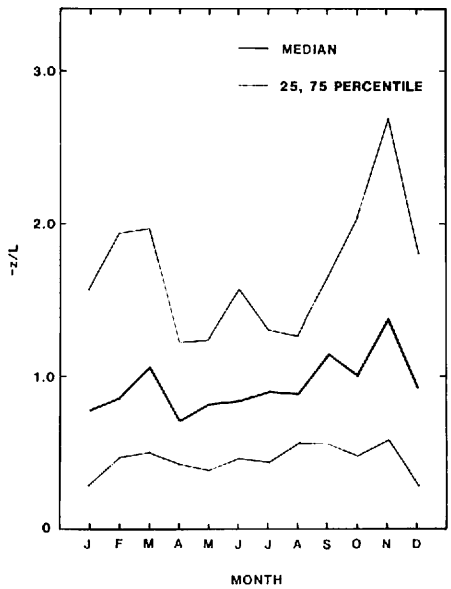

Fig. 21 Seasonal variation of z/L expressed by 25 and 75 percentiles, and the median.

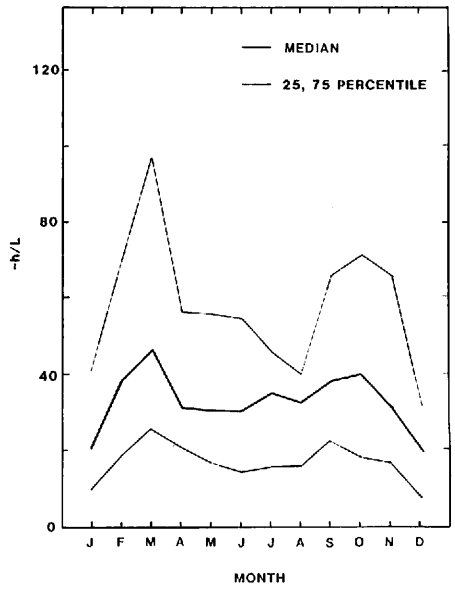

Fig. 22 Same as Fig. 21, but for h/L.

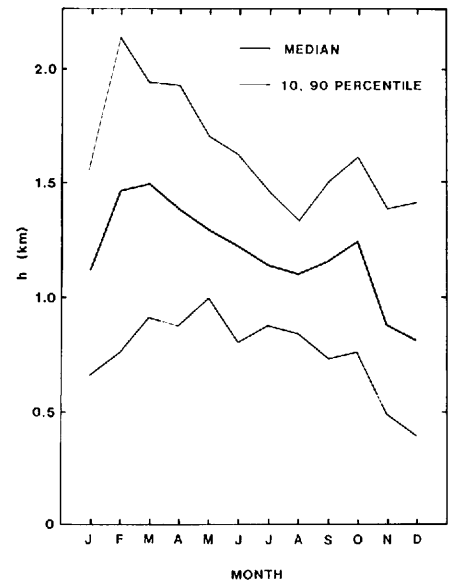

Fig. 23 Seasonal variation of h expressed by 10 and 90 percentiles, and the median.

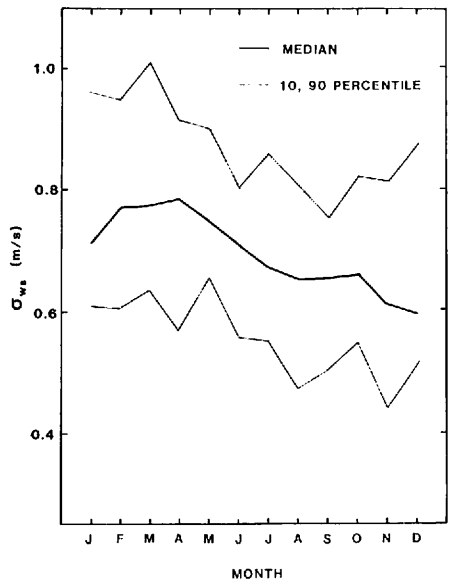

Fig. 24 Same as Fig. 23, but for σ_{ws}.

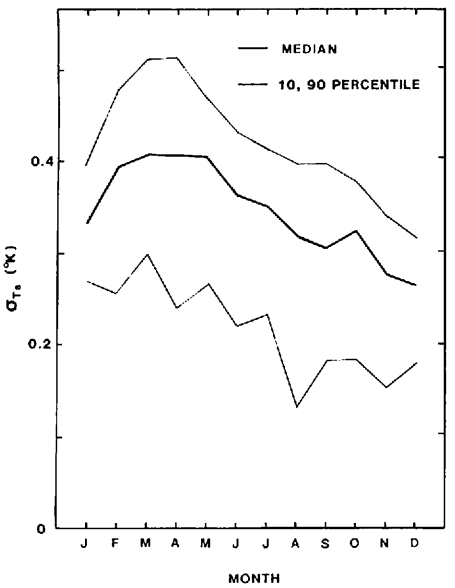

Fig. 25 Same as Fig. 23, but for σ_{Ts}.

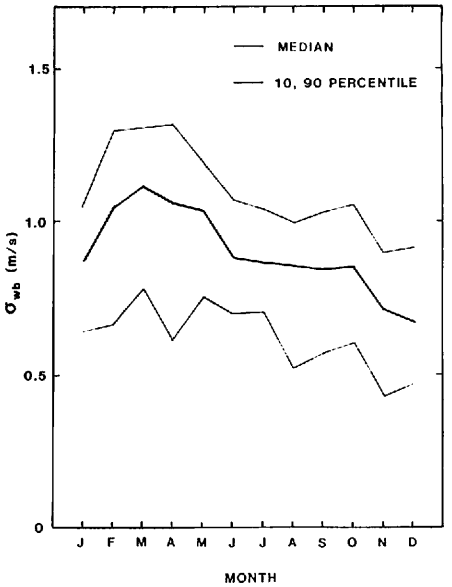

Fig. 26 Same as Fig. 23, but for σ_{wb}.

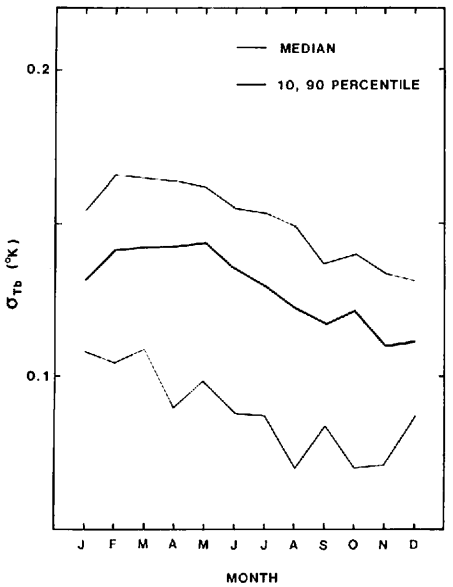

Fig. 27 Same as Fig. 23, but for σ_{Tb}

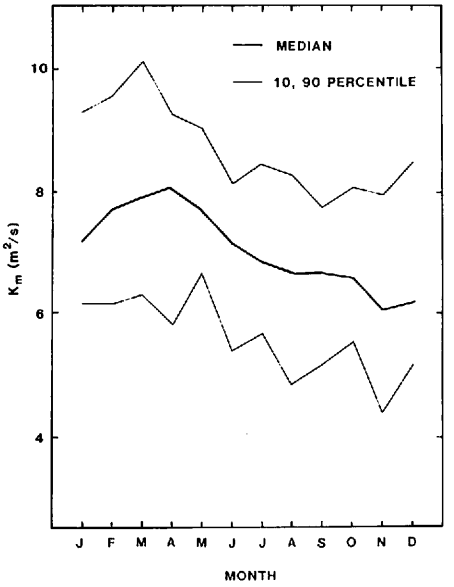

Fig. 28 Same as Fig. 23, but for K_m.

Seasonal variations of σ_{ws}, σ_{Ts},σ_{wb}, σ_{Tb} are shown in Figs. 24, 25, 26, and 27. Generally there is a tendency for the standard deviations of temperature and vertical velocity to be largest in spring and thereafter decrease gradually. Since the calculation methods and statistical treatments are different, it is difficult to compare these results with the results obtained by Gamo (1983). However, results are similar in magnitude and seasonal variation pattern.

Seasonal variation patterns of K_m and K_h are similar to each other, and like the variance terms, largest in spring and smallest in winter, as have shown in Figs. 28 and 29.

Maximum and minimum values of the median among 12 months for quantities described above are summarized in Table 13. Details of the results are presented in APPENDIX.

Table 13 Maximum and minimum values among medians for 12 months. Median values are taken at 12:30 LST except for the mixed layer height. Medians of the mixed layer height are taken at 14:30 LST.

	Median			
	Maximum		Minimum	
$-z/L$	1.36	(Nov.)	0.691	(Apr.)
$-h/L$	46.4	(Mar.)	20.1	(Dec.)
u_* (m/s)	0.427	(Apr.)	0.261	(Nov.)
w_* (m/s)	1.95	(Mar.)	1.18	(Dec.)
h (m)	1,490	(Mar.)	816	(Dec.)
σ_{ws} (m/s)	0.787	(Apr.)	0.599	(Dec.)
σ_{Ts} (°K)	0.408	(Mar.)	0.262	(Dec.)
σ_{wb} (m/s)	1.11	(Mar.)	0.667	(Dec.)
σ_{Tb} (°K)	0.143	(May)	0.110	(Nov.)
K_m (m^2/s)	8.03	(Apr.)	6.04	(Nov.)
K_h (m^2/s)	15.8	(Mar.)	12.5	(Dec.)

4.4 Evolution of the convective boundary layer in the daytime

Diurnal variations of the structure of the convective boundary layer were obtained daily. However, to show representative values, we use the median as a monthly basis. Four months are selected as examples to describe diurnal variation; February, May, August, November. These months are particulary interesting and remarkably different from each other.

Diurnal variation of u_* is shown in Fig. 30. The value of u_* increases in the afternoon. Generally, diurnal variation of w_* has a tendency to increase slowly and peak between 12:30 LST and 13:30 LST, and then decrease rapidly (Fig. 31).

Fig. 32 shows diurnal variation of z/L at 25 m. It is striking that in the surface layer, the stability varies notably during the course of a day, and also that the layer is more unstable in the morning hours than in the afternoon. In the case of the boundary layer, the stability is most unstable near noon, with a maximum value of $-h/L$ appearing at 12:30 LST in February (Fig. 33). Features of diurnal variation of stability in the boundary layer are quite different as compared to that of the surface layer.

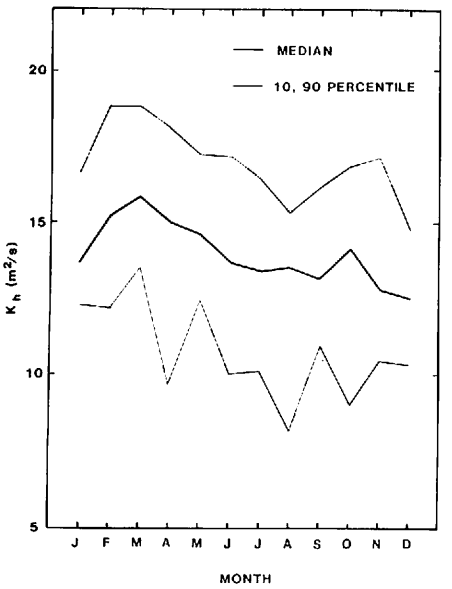

Fig. 29 Same as Fig. 23, but for K_h.

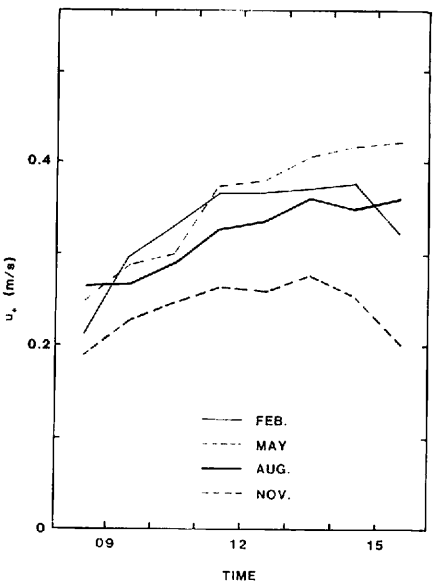

Fig. 30 Diurnal variation of u_* for selected months; Feb., May, Aug., and Nov.. The value of monthly u_* is expressed by the median.

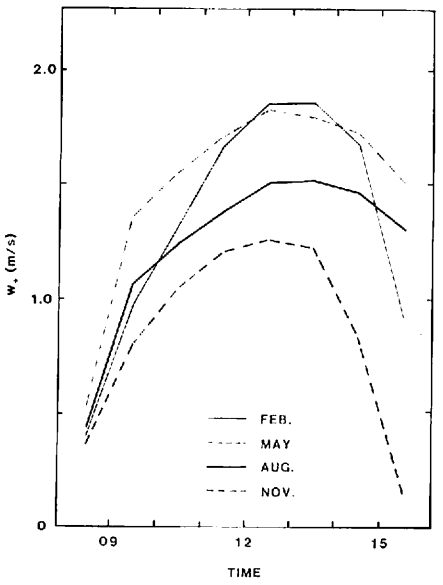

Fig. 31 Same as Fig. 30, but for w_*.

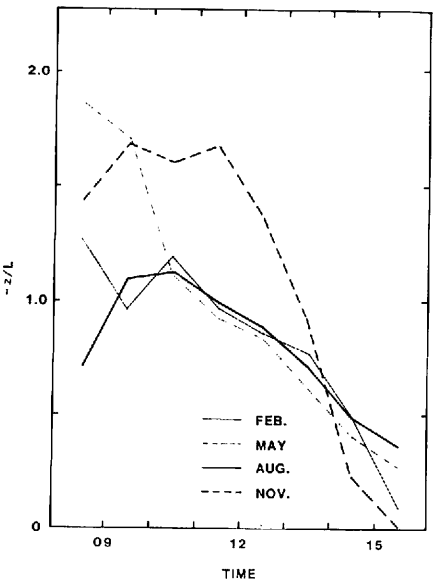

Fig. 32 Same as Fig. 30, but for z/L.

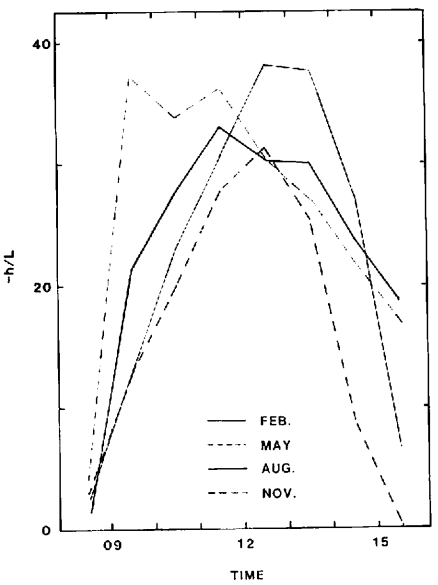

Fig. 33 Same as Fig. 30, but for h/L.

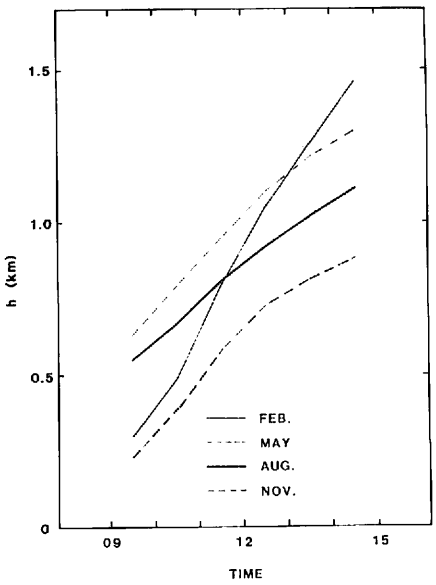

Fig. 34 Same as Fig. 30, but for h.

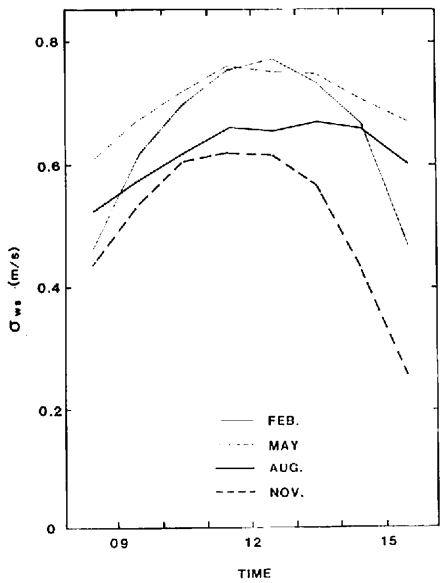

Fig. 35 Same as Fig. 30, but for σ_{ws}.

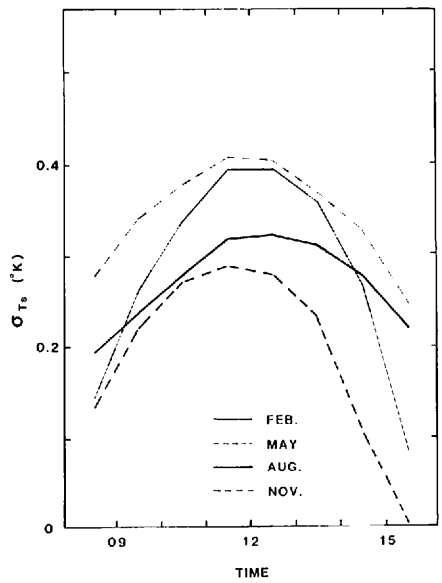

Fig. 36 Same as Fig. 30, but for σ_{Ts}.

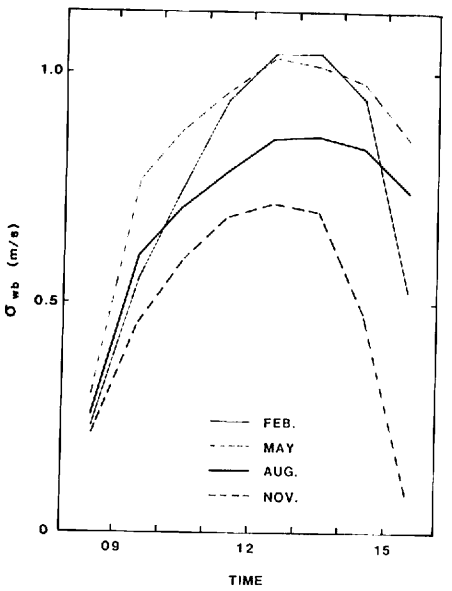

Fig. 37 Same as Fig. 30, but for σ_{wb}.

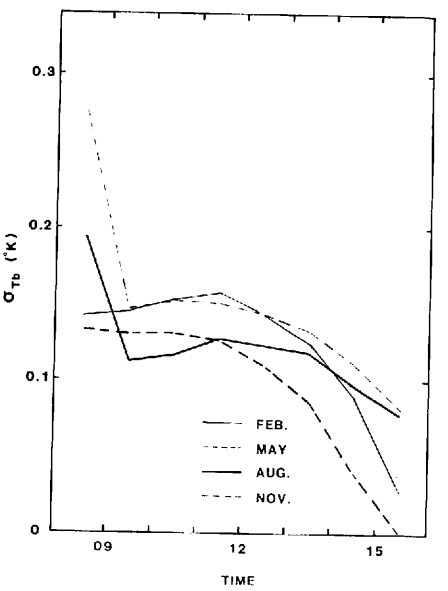

Fig. 38 Same as Fig. 30, but for σ_{Tb}.

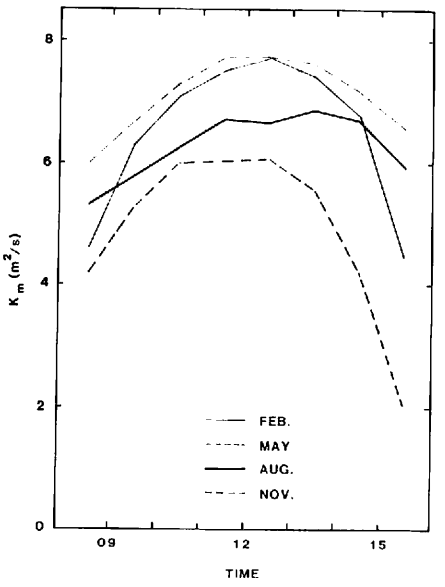

Fig. 39 Same as Fig. 30, but for K_m.

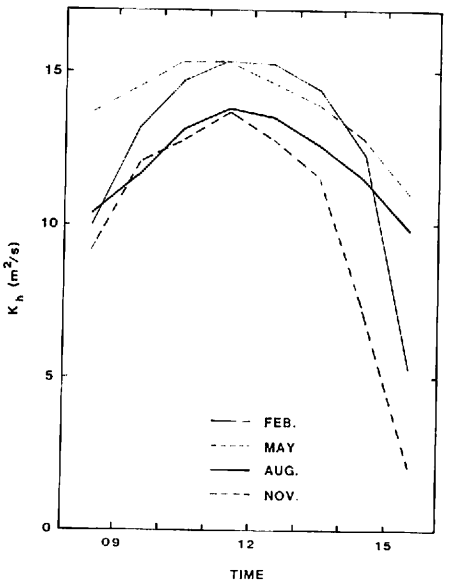

Fig. 40 Same as Fig. 30, but for K_h.

Developing features of the mixed layer are remarkably different by month (Fig. 34). We take initial value of h at 08:30 LST as being a constant, and when a surface inversion starts to form, h become meaningless. Therefore h at 08:30 and 15:30 LST are excluded from Fig. 34.

In February, h is relatively low in morning hours but develops rapidly, and in August, is relatively high in the morning hours, but lower than the other months in the afternoon because of a slow developing rate. The mean developing rate of the mixed layer from 09:30 to 14:30 LST is presented in Table 14.

Table 14 Mean developing rate of mixed layer from 09:30 to 14:30 LST.

Month	Jan.	Feb.	Mar.	Apr.	May	Jun.	Jul.	Aug.	Sep.	Oct.	Nov.	Dec.
$\partial h/\partial t$ (m/hour)	187	231	181	154	134	140	119	111	128	179	130	131

There is a trend for σ_{ws} to be largest near noon and small in morning and afternoon hours (Fig. 35). It is interesting that maximum values of σ_{ws} occurred before noon in November, and occurred after noon in August.

The diurnal variation pattern of σ_{Ts} is similar to σ_{ws} (Fig. 36).

As shown in Fig. 37, the diurnal variation pattern of σ_{wb} is similar to that of w_*.

The diurnal variation of σ_{Tb} shows a peculiar pattern (Fig. 38); large before noon, then gradually decreases in the afternoon. It is especially large at 08:30 LST for May and August.

Maximum values of K_m occurred at 12:30 LST, except for August, when maximums occurred at 13:30 LST (Fig. 39). On the other hand, maximum values of K_h occurred at 11:30 for all months (Fig. 40).

It is worth remarking that maximum values of K_m occurred in the afternoon and that maximum values of K_h occurred before noon.

Hourly values described above for all months are presented in APPENDIX.

4.5 Relationships between structure of convective boundary layer and synoptic conditions

We surveyed the relationships between seasonal variation of structure of the convective boundary layer and synoptic conditions; $\gamma_{500\text{-}1500}$ and sky condition.

Seasonal variation of $\gamma_{500\text{-}1500}$ is shown in Fig. 41. It can be seen that $\gamma_{500\text{-}1500}$ is large in summer, with a maximum is 5.9°K/km in July. On the other hand, it is small in winter and the minimum is 3.1°K/km, in February.

From Figs. 23 and 41, it is clear that h is inversely correlated with the potential temperature gradient. Seasonal variation of $\gamma_{500\text{-}1500}$ is related to the air mass types and their occurring frequency.

Fig. 42 shows relative frequency of the six air mass types described in Section 4.1. Frequency of cPs is high in winter and that of mT is high in summer. Migratory anticyclones, M, occur thoughout the year. Mean value of $\gamma_{500\text{-}1500}$ for the six air mass types are shown in Fig. 43. Mean value of $\gamma_{500\text{-}1500}$ for the continental air mass is small and that of the maritime air mass is large. Mean value of $\gamma_{500\text{-}1500}$ for the migratory anticyclone is an intermediate value.

Mean profiles of the potential temperature gradient for air mass types which occurred most

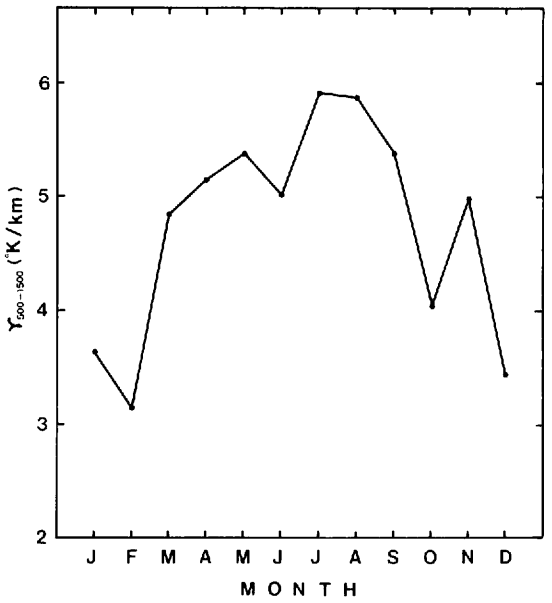

Fig. 41 Seasonal variation of $\gamma_{500\text{-}1500}$.

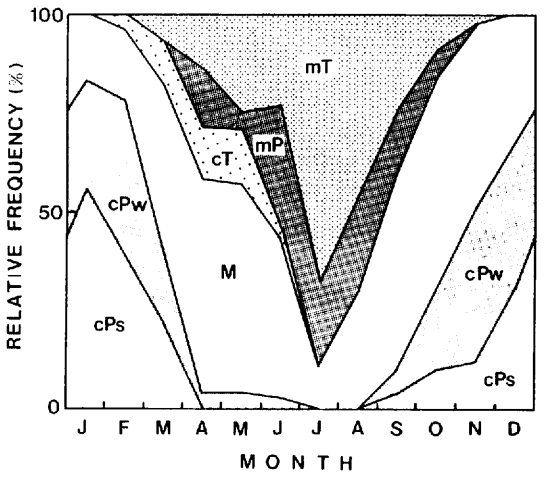

Fig. 42 Relative frequencies of the six air mass types.

frequently in a month, are presented together with the percentile values of h at 14:30 LST in Fig. 44. The role of a strong inversion layer to the development of the mixed layer is clearly seen in May and November in the air mass type of M, and in August in the air mass type of mT.

Development of the mixed layer is suppressed by a strong inversion layer, perhaps a subsidence inversion especially in summer. The fact that day to day variations of h are large in winter

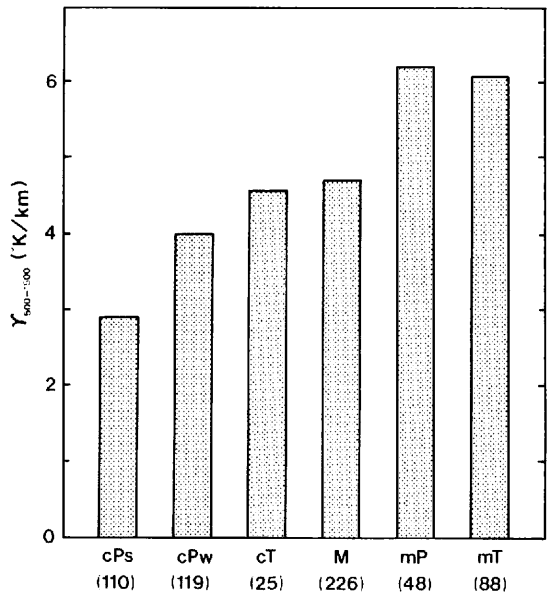

Fig. 43 Mean values of $\gamma_{500\text{-}1500}$ for the six air mass types. Values in the parenthesis indicate the number of days.

and small in summer may be explained from the potential temperature gradient and the existence of a strong inversion layer.

Fig. 45 shows a comparison of quantities in the convective boundary layer between fair weather conditions and cloudy conditions. In general, because of strong insolation, convection is more active under fair weather conditions than under cloudy conditions. However, stabilities are more unstable under cloudy conditions in February and May than under fair weather conditions. Except for August, $\gamma_{500\text{-}1500}$ is larger for cloudy conditions than for fair weather conditions.

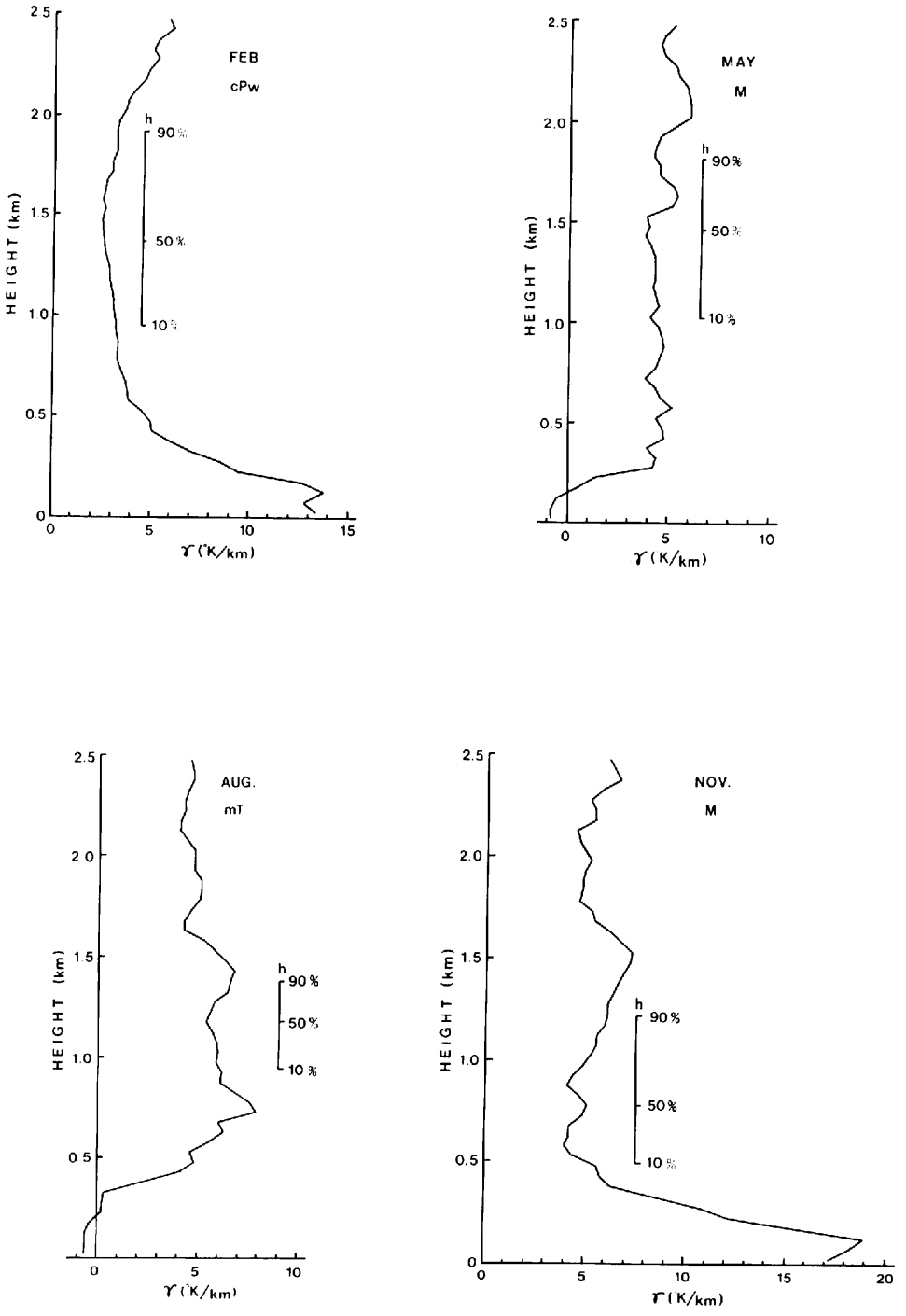

Fig. 44 Mean profile of the potential temperature gradient for the air mass type which has the highest frequency in a month. Bars with 10, 50, and 90% express the percentile values of the mixed layer height at 14:30 LST corresponding to the highest frequency air mass type.

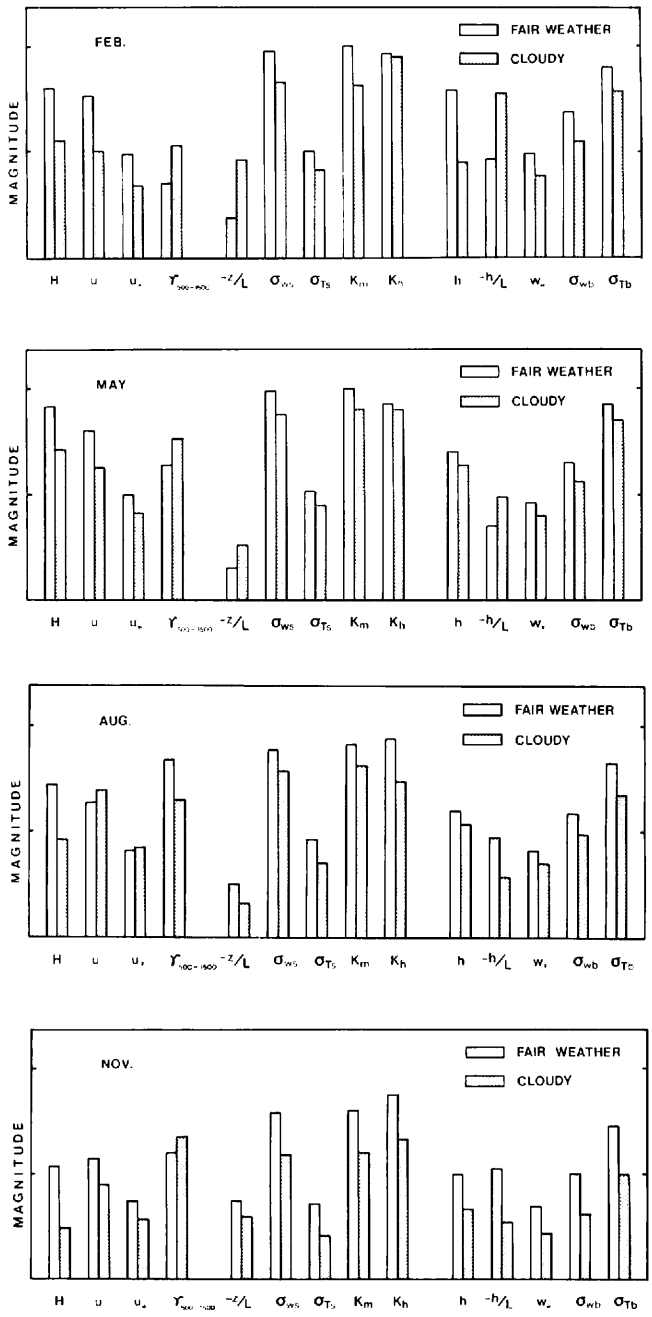

Fig. 45 Comparison of parameters in the convective boundary layer between fair weather conditions and cloudy conditions. Ordinate represents positive magnitude, and scale is arbitrarily adjusted for each parameter.

CHAPTER V

CONCLUSIONS

In the present study, a model which can estimate parameters in the convective boundary layer using routine meteorological observation data was developed, and climatological aspects of the convective boundary layer were studied by applying this model.

The jump model was modified for application to various weather conditions. In order to consider the effect of mechanical convection on the jump model, the entrainment ratio was parameterized by use of the friction velocity. Large scale vertical motion affects the developing velocity of the mixed layer and causes variation in the potential temperature profile. Therefore, these effects were considered in the modification of the jump model.

From the results of the sensitivity test of the modified jump model, it becomes clear that effects of mechanical convection and large scale vertical motion become important in specific cases. Thus, it is necessary to modify the jump model to accommodate mechanical convection and large scale vertical motion, especially for the purpose of climatological analysis which cover a broad range of weather conditions.

The modified jump model was evaluated with the data sets of the Wangara experiment and field observations which were carried out at Tsukuba. The evaluation of the model shows that the results are improved by modification.

An empirical equation for estimating the surface heat flux was determined. The required input data are air temperature and net radiation. Heat flux estimated by the empirical equation was compared with the data observed with the meteorological tower at the Meteorological Research Institute. We obtained good agreement between estimates and observations. Root mean square error (RMSE) is 24 W/m^2.

A scheme for the estimation of the friction velocity and the Monin-Obukhov length, using wind speed at a single height and the surface heat flux obtained from the empirical equation, was presented. The friction velocity estimated by this scheme agrees fairly well with observed value. RMSE of the friction velocity is 0.072 m/s. However, estimated Monin-Obukhov length does not fit observed value as well as does the case of the friction velocity. Since the Monin-Obukhov length is proportional to the cubic of the friction velocity, and error in the friction velocity is exaggerated.

Calculated values of the standard deviation of vertical velocity and temperature in the surface layer were compared with observed values. Results show that calculations agree well with observations. However, there is a trend that the observed values are to be slightly smaller than the calculated values. It may be considered that observed variances may fail to include the values of low frequency.

In order to analyze the seasonal and diurnal variation of the structure of the convective boundary layer in the daytime at Tsukuba, the schemes described in Chapter II and III were applied for 3 years. The results are summarized as follows.

(1) The velocity scale in the boundary layer is largest in March and smallest in December. Refering to the seasonal variation of the velocity scale, it is clear that convection is most intense in spring.

(2) In the daytime, stability of the surface layer is most unstable in November, and for the boundary layer, most unstable in March. Features of diurnal variation of stability in the boundary layer are quite different as compared to stability in the surface layer. The surface layer is more unstable in morning hours than in the afternoon. In the case of the boundary layer, stability is most unstable near noon.

(3) The mixed layer height shows large variation throughout the year. There are two peaks in seasonal variation patterns; spring and autumn. The mixed layer is highest in March, 1,490 m, and lowest in December, 816 m. Notably it is not so high in summer despite strong solar radiation. Development of the mixed layer during the daytime is most rapid in February and slowest in August.

(4) Generally, there is a tendency for the standard deviations of temperature and vertical velocity to be largest in spring and thereafter decrease gradually. Diurnal variation patterns show that maximum values are occurred between 11:30 LST and 13:30 LST, excluding the standard deviation of temperature in the boundary layer, occurring in the morning.

(5) The potential temperature gradient for the layer between 500 m and 1,500 m varies throughout the year. It is large in summer and small in winter. This feature is related to air mass type, *i.e.*, potential temperature gradient of continental air mass in winter is small and that of maritime air mass in summer is large.

(6) The mixed layer height is inversely correlated with the potential temperature gradient in the stable layer above the mixed layer. Development of the mixed layer is suppressed by a strong inversion layer, perhaps subsidence inversion, especially in summer.

(7) Convection is more active under fair weather conditions than under cloudy conditions. However, on occasion, stability is more unstable under cloudy condition than during fair weather.

Finally, the following should be noted. The model developed in the present study can be applied not only to climatological study of the convective boundary layer, but also to air pollution problems or to the study of turbulence in the boundary layer, as a simple method which requires routine meteorological observation data only; net radiation, air temperature, wind speed at single height, and morning radiosonde sounding.

ACKNOWLEDGEMENTS

The author wishes to express his sincere gratitude to his academic adviser, Dr. Masatoshi M. Yoshino, Professor at the Institute of Geoscience, the University of Tsukuba, for his guidance and support in the present study. Special thanks are extended to Professors Takeshi Kawamura and Toshie Nishizawa for their suggestions.

The author gratefully acknowledges guidance and encouragement from Dr. Tatsuo Hanafusa of the Meteorological Research Institute. In addition, the author wishes to acknowledge the kind assistance provided by the members of the Division of Physical Meteorology, Meteorological Research Institute. Thanks are due to Dr. Yousay Hayashi, Miss Taiko Kudoh, and Mr. Robert C. Backstrom for support in preparing this thesis.

The field observation was performed with the courtesy of the Meteorological Research Institute and the Tateno Aerological Station. To perform this study, the data observed at the Environmental Research Center, the University of Tsukuba were also used.

REFERENCES

Ball, F.K. (1960): Control of inversion height by surface heating. *Quart. J.R. Met. Soc.*, **86**, 483–494.

Barry, R.G. and Perry, A.H. (1973): *Synoptic climatology*. Methuen & Co., Ltd., 555 pp.

Benkley, C.W. and Schulman, L.L. (1979): Estimating hourly mixing depths from historical meteorological data. *J. Appl. Meteor.*, **18**, 772–780.

Businger, J.A., Wyngaard, J.C., Izumi, Y. and Bradley, E. F. (1971): Flux-profile relationships in the atmospheric surface layer. *J. Atmos. Sci.*, **28**, 181–189.

Carson, D.J. (1973): The development of a dry inversion-caped convectively unstable boundary layer. *Quart. J.R. Met. Soc.*, **99**, 450–467.

Cattle, H. and Weston, K. (1974): The determination of large scale motion by a modified isentropic technique. *Met. Mag.*, **103**, 82–89.

Caughey, S.J. and Palmer, S.G. (1979): Some aspects of turbulence structure through the depth of the convective boundary layer. *Quart. J.R. Met. Soc.*, **105**, 811–827.

Clarke, R.H., Dyer, A.J., Brook, R.R., Reid, D. G. and Troup, A.J. (1971): The Wangara experiment: Boundary layer data. *Tech. Pap.* 19, *Div. Meteor. Phys.*, CSIRO, Aspendale, Victoria, Australia, 341 pp.

De Bruin, H.A. and Holtslag, A.A.M. (1982): A simple parameterization of the surface fluxes of sensible and latent heat during daytime compared with the Penman-Monteith concept. *J. Appl. Meteor.*, **21**, 1610–1621.

_____ and Keijman, J.Q. (1979): The Priestley-Taylor evaporation model applied to a large shallow lake in the Netherlands. *J. Appl. Meteor.*, **18**, 898–903.

Deardorff, J.W. (1972): Parameterization of the planetary boundary layer for use in general circulation models. *Mon. Wea. Rev.*, **100**, 93–106.

_____ (1973): An explanation of anomalously large Reynolds stresses within the convective planetary boundary layer. *J. Atmos. Sci.*, **30**, 1070–1076.

Driedonks, A.G.M. (1982): Models and observations of the growth of the atmospheric boundary layer. *Bound.-Layer Meteor.*, **23**, 283–306.

Fujitani, T. (1983): Seasonal variations of thermal diffusivity in the atmospheric boundary layer. *Tenki*, **30**, 603–609.**

Gamo, M. (1981): The lapse rate of the stable layer capping the mixed layer. *Pollution*, **16**, 315– 321.*

_____ (1983): Annual variation of the mixed layer structure at Tsukuba. *Pollution*, **18**, 51–68.*

_____ and Yokoyama, O. (1979): Growth of the mixing depth and the diurnal variation of vertical profiles of temperature and turbulence characteristics in the mixing layer. *J. Met. Soc. Japan*, **57**, 159–172.

Hanafusa, T., Fujitani T., Banno, N. and Uozu, H. (1979): On the meteorological tower and its observational system at Tsukuba Science City. *Tech. Rep. MRI*, 3, 50 pp.*

Holtslag, A.A. M. and Van Ulden, A.P. (1983): A simple scheme for daytime estimates of the surface fluxes from routine weather data. *J. Clim. Appl. Meteor.*, **22**, 517–529.

Holzworth, G.C. (1964): Estimates of mean maximum mixing depths in the contiguous United States. *Mon. Wea. Rev.*, **92**, 235–242.

Lenschow, D.H. and Johnson, W.B. (1968): Concurrent airplaine and balloon measurements of atmospheric boundary layer structure over a forest. *J. Appl. Meteor.*, **7**, 79–89.

Lilly, D.K. (1968): Models of cloud-topped mixed layers under a strong inversion. *Quart. J.R. Met. Soc.*, **94**, 292–309.

Mahrt, M. and Lenschow, D.H. (1976): Growth dynamics of the convectively mixed layer. *J. Atmos. Sci.*, **33**, 41–51.

Meteorological Research Institute (1983): Northern hemispheric and Asia fine-mesh numerical weather prediction model and objective analysis system of JMA used in 1982. *Computer center report*, 29, 93 pp.*

Monteith, J.L. (1981): Evaporation and surface temperature. *Quart. J.R. Met. Soc.*, **107**, 1–27.

Naito, K., Hanafusa, T. and Fujitani, T. (1983): On spatial structures of high winds. *U.S.-Japan panel on wind and seismic effects.* UJNR, Tsukuba, May, 17–20, 1983.

Norton, C.L. and Hoidale, G.B. (1976): The diurnal variation of mixing height by season over White Sands Missile Range, New Mexico. *Mon. Wea. Rev.*, **104**, 1317–1320.

Panofsky, H.A. and Mazzola, C. (1971): Variances and spectra of vertical velocity just above the surface layer. *Bound.-Layer Meteor.*, **2**, 30–37.

——— , Tennekes, H., Lenschow, D.H. and Wyngaard, J.C. (1977): The characteristics of turbulent velocity components in the surface layer under convective conditions. *Bound.-Layer Meteor.*, **11**, 355–361.

Paulson, C.A. (1970): The mathematical representation of wind speed and temperature profiles in the unstable atmospheric surface layer. *J. Appl. Meteor.*, **9**, 857–861.

Priestley, C.H. and Taylor, R.J. (1972): On the assessment of surface heat flux and evaporation using large-scale parameters. *Mon. Wea. Rev.*, **106**, 81–92.

Stull, R.B. (1973): Inversion rise model based on penetrative convection. *J. Atmos. Sci.*, **30**, 1092–1099.

——— (1976): The energetics of entrainment across a density interface. *J. Atmos. Sci.*, **33**, 1260–1267.

Sugiura, S. (1972): Maximum mixing depth at Tokyo and its surroundings and correlation between relative concentration and SO_2 at Tokyo. *Tenki*, **19**, 606–612.**

Tennekes, H. (1973): A model for the dynamics of the inversion above a convective boundary layer. *J. Atmos. Sci.*, **30**, 558–567.

Wyngaard, J.C., Cote, O.R. and Izumi, Y. (1971): Local free convection, similarity, and the budgets of shear stress and heat flux. *J. Atmos. Sci.*, **28**, 1171–1182.

Yamada, T. and Berman, S. (1979): A critical evaluation of a simple mixed layer model with penetrative convection. *J. Appl. Meteor.*, **18**, 781–786.

Yoshino, M.M. (1968): Pressure pattern calendar of East Asia. *Met. Rdsch.*, **21**, 162–169.

——— and Kai, K. (1974): Pressure pattern calendar of East Asia, 1941–1970, and its climatological summary. *Climatological Notes*, 16, 1–71.

Yu, T.W. (1977): Parameterrization of surface evaporation rate for use in numerical modeling. *J. Appl. Meteor.*, **16**, 393–400.

---

* In Japanese with English abstract

** In Japanese with Japanese abstract

APPENDIX

Median values of quantities in the convective boundary layer for 12 months.

1) u_*

(Unit; m/s)

Month \ Time	08:30	09:30	10:30	11:30	12:30	13:30	14:30	15:30
Jan.	0.17	0.28	0.32	0.35	0.38	0.39	0.37	0.28
Feb.	0.21	0.30	0.33	0.37	0.37	0.37	0.38	0.32
Mar.	0.27	0.31	0.34	0.36	0.38	0.40	0.42	0.41
Apr.	0.25	0.30	0.34	0.38	0.43	0.42	0.43	0.44
May	0.25	0.29	0.33	0.37	0.38	0.41	0.42	0.42
Jun.	0.24	0.27	0.28	0.31	0.33	0.38	0.42	0.39
Jul.	0.25	0.27	0.31	0.34	0.34	0.37	0.38	0.36
Aug.	0.26	0.27	0.29	0.33	0.34	0.36	0.35	0.36
Sep.	0.24	0.27	0.30	0.30	0.32	0.34	0.37	0.35
Oct.	0.22	0.27	0.27	0.30	0.32	0.33	0.34	0.28
Nov.	0.19	0.23	0.25	0.26	0.26	0.28	0.25	0.20
Dec.	0.18	0.24	0.27	0.30	0.30	0.27	0.20	0.17

2) w_*

(Unit; m/s)

Month \ Time	08:30	09:30	10:30	11:30	12:30	13:30	14:30	15:30
Jan.	0.25	0.73	1.09	1.36	1.53	1.45	1.21	1.61
Feb.	0.40	0.97	1.32	1.66	1.85	1.85	1.66	0.93
Mar.	0.49	1.29	1.57	1.83	1.95	1.89	1.75	1.40
Apr.	0.54	1.38	1.63	1.77	1.88	1.89	1.81	1.54
May	0.54	1.36	1.55	1.70	1.82	1.79	1.72	1.50
Jun.	0.49	1.17	1.32	1.51	1.55	1.65	1.56	1.42
Jul.	0.47	1.14	1.32	1.45	1.53	1.52	1.53	1.44
Aug.	0.44	1.06	1.25	1.39	1.50	1.52	1.47	1.31
Sep.	0.45	1.08	1.29	1.38	1.49	1.53	1.46	1.17
Oct.	0.45	0.97	1.22	1.40	1.50	1.54	1.35	0.63
Nov.	0.38	0.80	1.05	1.21	1.26	1.23	0.82	0.15
Dec.	0.28	0.65	0.89	1.09	1.18	1.11	0.68	0.14

3) $-z/L$

Month \ Time	08:30	09:30	10:30	11:30	12:30	13:30	14:30	15:30
Jan.	0.42	1.08	1.04	0.94	0.78	0.57	0.31	0.00
Feb.	1.27	0.96	1.18	0.96	0.86	0.76	0.48	0.09
Mar.	1.11	1.07	1.34	1.12	1.06	0.70	0.40	0.20
Apr.	1.44	1.20	1.03	0.89	0.69	0.58	0.41	0.27
May	1.85	1.71	1.11	0.92	0.83	0.62	0.40	0.27
Jun.	1.65	1.42	1.45	1.23	0.85	0.62	0.48	0.34
Jul.	1.37	1.35	1.27	1.02	0.90	0.77	0.53	0.39
Aug.	0.71	1.09	1.12	0.99	0.88	0.79	0.48	0.36
Sep.	1.09	1.25	1.04	0.94	1.13	0.89	0.56	0.29
Oct.	1.39	1.15	1.42	1.18	0.99	0.84	0.49	0.08
Nov.	1.43	1.68	1.60	1.67	1.36	0.92	0.23	0.00
Dec.	0.69	1.09	1.24	0.93	0.92	0.81	0.18	0.01

4) $-h/L$

Month \ Time	08:30	09:30	10:30	11:30	12:30	13:30	14:30	15:30
Jan.	0.84	7.7	12.9	17.2	21.0	21.7	13.4	0.1
Feb.	2.55	13.0	23.1	30.5	38.1	37.5	27.2	6.4
Mar.	2.22	21.4	33.5	44.6	46.4	35.1	23.4	13.1
Apr.	2.88	24.8	35.5	34.3	31.1	29.7	22.0	15.1
May	3.71	36.9	33.7	36.0	30.2	27.1	21.6	16.7
Jun.	3.31	31.7	31.7	32.7	30.6	26.0	20.3	18.1
Jul.	2.73	27.5	33.9	35.3	34.8	32.2	27.3	17.7
Aug.	1.42	21.3	27.7	33.1	32.7	29.9	23.4	18.4
Sep.	2.18	18.5	24.7	29.8	38.2	34.2	28.3	14.0
Oct.	2.78	19.1	27.2	36.1	39.6	36.1	26.2	4.3
Nov.	2.86	13.0	20.0	27.8	31.2	25.2	8.8	0.1
Dec.	1.39	6.3	11.8	15.4	20.1	18.4	6.8	0.2

5) h

(Unit; m)

Month \ Time	09:30	10:30	11:30	12:30	13:30	14:30	15:30
Jan.	185	378	600	870	1,050	1,120	1,150
Feb.	304	492	791	1,050	1,260	1,460	1,520
Mar.	584	865	1,060	1,220	1,380	1,490	1,520
Apr.	620	849	1,030	1,200	1,300	1,390	1,440
May	628	791	945	1,100	1,220	1,300	1,390
Jun.	529	685	816	935	1,090	1,230	1,300
Jul.	546	697	797	906	1,040	1,140	1,230
Aug.	553	664	796	924	1,020	1,110	1,170
Sep.	520	695	834	966	1,080	1,160	1,240
Oct.	347	554	788	936	1,090	1,240	1,280
Nov.	234	385	584	715	813	883	919
Dec.	159	168	420	610	739	816	840

6) σ_{ws}

(Unit; m/s)

Month \ Time	08:30	09:30	10:30	11:30	12:30	13:30	14:30	15:30
Jan.	0.32	0.55	0.65	0.71	0.71	0.66	0.57	0.35
Feb.	0.46	0.62	0.70	0.76	0.77	0.74	0.67	0.47
Mar.	0.56	0.68	0.73	0.77	0.77	0.75	0.71	0.61
Apr.	0.61	0.68	0.73	0.77	0.79	0.78	0.73	0.66
May	0.61	0.68	0.72	0.76	0.75	0.75	0.71	0.67
Jun.	0.55	0.60	0.65	0.70	0.71	0.73	0.70	0.65
Jul.	0.55	0.59	0.64	0.67	0.68	0.67	0.67	0.60
Aug.	0.52	0.58	0.62	0.66	0.65	0.67	0.66	0.60
Sep.	0.52	0.58	0.64	0.64	0.66	0.66	0.61	0.54
Oct.	0.51	0.59	0.63	0.64	0.67	0.65	0.58	0.38
Nov.	0.43	0.54	0.60	0.62	0.61	0.57	0.43	0.26
Dec.	0.36	0.51	0.58	0.62	0.60	0.54	0.36	0.21

7) σ_{Ts}

(Unit; °K)

Month \ Time	08:30	09:30	10:30	11:30	12:30	13:30	14:30	15:30
Jan.	0.06	0.20	0.28	0.33	0.33	0.28	0.17	0.00
Feb.	0.14	0.26	0.34	0.39	0.39	0.36	0.26	0.08
Mar.	0.22	0.31	0.37	0.42	0.41	0.37	0.31	0.19
Apr.	0.28	0.34	0.39	0.41	0.41	0.39	0.33	0.23
May	0.28	0.34	0.38	0.41	0.40	0.37	0.33	0.25
Jun.	0.23	0.28	0.32	0.36	0.36	0.35	0.29	0.24
Jul.	0.22	0.26	0.30	0.33	0.35	0.31	0.30	0.22
Aug.	0.19	0.24	0.28	0.32	0.32	0.31	0.28	0.22
Sep.	0.20	0.27	0.30	0.34	0.34	0.31	0.27	0.17
Oct.	0.20	0.26	0.30	0.33	0.32	0.29	0.21	0.05
Nov.	0.13	0.22	0.27	0.29	0.28	0.23	0.10	0.00
Dec.	0.07	0.18	0.25	0.27	0.26	0.20	0.08	0.00

8) σ_{wb}

(Unit; m/s)

Month \ Time	08:30	09:30	10:30	11:30	12:30	13:30	14:30	15:30
Jan.	0.14	0.41	0.62	0.77	0.87	0.82	0.69	0.09
Feb.	0.22	0.55	0.75	0.94	1.04	1.04	0.94	0.52
Mar.	0.28	0.73	0.89	1.04	1.11	1.07	0.99	0.79
Apr.	0.31	0.78	0.92	1.00	1.06	1.07	1.03	0.87
May	0.30	0.77	0.88	0.96	1.03	1.01	0.98	0.85
Jun.	0.28	0.66	0.75	0.85	0.88	0.94	0.88	0.80
Jul.	0.27	0.65	0.75	0.82	0.86	0.86	0.87	0.82
Aug.	0.25	0.60	0.71	0.79	0.85	0.86	0.83	0.74
Sep.	0.25	0.61	0.73	0.78	0.84	0.87	0.82	0.66
Oct.	0.26	0.55	0.69	0.79	0.85	0.87	0.77	0.36
Nov.	0.21	0.45	0.60	0.68	0.71	0.70	0.46	0.08
Dec.	0.16	0.37	0.50	0.62	0.67	0.63	0.38	0.08

9) σ_{Tb}

(Unit; °K)

Month \ Time	08:30	09:30	10:30	11:30	12:30	13:30	14:30	15:30
Jan.	0.06	0.13	0.15	0.15	0.13	0.10	0.06	0.00
Feb.	0.14	0.14	0.15	0.16	0.14	0.12	0.09	0.03
Mar.	0.22	0.14	0.15	0.15	0.14	0.13	0.11	0.06
Apr.	0.28	0.14	0.15	0.15	0.14	0.13	0.11	0.07
May	0.28	0.14	0.15	0.15	0.14	0.13	0.11	0.08
Jun.	0.23	0.12	0.14	0.14	0.14	0.13	0.11	0.08
Jul.	0.22	0.12	0.12	0.13	0.13	0.11	0.11	0.08
Aug.	0.19	0.11	0.12	0.13	0.12	0.12	0.10	0.08
Sep.	0.20	0.11	0.12	0.12	0.12	0.10	0.09	0.05
Oct.	0.20	0.13	0.13	0.13	0.12	0.11	0.07	0.02
Nov.	0.13	0.13	0.13	0.13	0.11	0.09	0.04	0.00
Dec.	0.07	0.11	0.13	0.13	0.11	0.08	0.03	0.00

10) K_h

(Unit; m^2/s)

Month \ Time	08:30	09:30	10:30	11:30	12:30	13:30	14:30	15:30
Jan.	3.09	5.63	6.57	7.09	7.20	6.69	5.72	2.78
Feb.	4.60	6.28	7.08	7.52	7.72	7.42	6.73	4.43
Mar.	5.63	6.78	7.33	7.85	7.88	7.45	7.11	6.03
Apr.	6.05	6.80	7.38	7.80	8.03	7.81	7.38	6.58
May	5.99	6.64	7.28	7.69	7.70	7.59	7.15	6.54
Jun.	5.50	5.99	6.46	6.91	7.16	7.31	7.03	6.50
Jul.	5.52	6.08	6.53	6.63	6.86	6.81	6.74	6.15
Aug.	5.30	5.78	6.23	6.72	6.65	6.83	6.68	5.96
Sep.	5.25	5.89	6.40	6.48	6.64	6.74	6.19	5.28
Oct.	5.00	5.88	6.26	6.48	6.53	6.54	5.86	3.46
Nov.	4.21	5.32	6.01	6.06	6.04	5.56	4.18	2.07
Dec.	3.52	5.13	5.83	6.20	6.13	5.43	3.66	1.70

11) K_m

(Unit; m^2/s)

Month \ Time	08:30	09:30	10:30	11:30	12:30	13:30	14:30	15:30
Jan.	5.50	11.0	13.1	13.7	13.7	12.5	9.29	2.80
Feb.	10.0	13.1	14.7	15.3	15.2	14.4	12.3	6.31
Mar.	12.0	14.4	15.3	16.1	15.8	14.9	12.7	9.56
Apr.	13.2	14.7	15.4	15.4	15.0	14.1	13.0	10.5
May	13.7	14.5	15.3	15.3	14.6	13.9	12.8	11.0
Jun.	12.6	13.2	14.0	14.5	13.7	13.4	11.7	10.3
Jul.	11.8	12.4	13.1	14.0	13.4	13.0	12.2	10.1
Aug.	10.3	11.6	13.1	13.8	13.5	12.6	11.5	9.81
Sep.	10.8	12.4	13.1	13.0	13.2	12.6	11.5	8.62
Oct.	11.2	12.3	13.8	13.9	14.1	12.7	10.4	5.08
Nov.	9.21	12.0	12.8	13.7	12.8	11.6	7.09	2.10
Dec.	6.29	10.2	12.2	12.9	12.5	11.0	6.27	1.75

Environmental Research Center Papers

No. 1 (1982) Kenji KAI: Statistical characteristics of turbulence and the budget of turbulent energy in the surface boundary layer. 54p.

No. 2 (1983) Hiroshi IKEDA: Experiments on bedload transport, bed forms, and sedimentary structures using fine gravel in the 4-meter-wide flume. 78p.

No. 3 (1983) Yousay HAYASHI: Aerodynamical properties of an air layer affected by vegetation. 54p.

No. 4 (1984) Shinji NAKAGAWA: Study on evapotranspiration from pasture. 87p.

No. 5 (1984) Fujiko ISEYA: An experimental study of dune development and its effect on sediment suspension. 56p.

No. 6 (1985) Akihiko KONDOH: Study on the groundwater flow system by environmental tritium in Ichihara region, Chiba Prefecture. 59p.

No. 7 (1985) Chong Bum LEE: Modelling and climatological aspects of convective boundary layer. 63p.

発行　　昭和60年3月25日

編集・発行者　筑波大学水理実験センター

〒305 茨城県新治郡桜村天王台1－1－1

TEL 0298 (53) 2532

印刷　株式会社 三　協　社

〒164 東京都中野区中央4－8－9